

## Catalyst poisoning influences from various functional groups of energy carriers towards electrochemical oxidation reactions on non-noble high-entropy alloy anodes in acidic media

Rafat Tahawy, Salma Aridha Muflihah, Kosuke Hara, Tatsuhiko Ohto, Hisanori Tanimoto, Tianshu Li, Mahmoud Abdelnabi, Samuel Jeong, Tomohiko Nishiuchi, Hajime Kimizuka, Akfany Hasdi Aimon & Yoshikazu Ito

**To cite this article:** Rafat Tahawy, Salma Aridha Muflihah, Kosuke Hara, Tatsuhiko Ohto, Hisanori Tanimoto, Tianshu Li, Mahmoud Abdelnabi, Samuel Jeong, Tomohiko Nishiuchi, Hajime Kimizuka, Akfany Hasdi Aimon & Yoshikazu Ito (24 Apr 2026): Catalyst poisoning influences from various functional groups of energy carriers towards electrochemical oxidation reactions on non-noble high-entropy alloy anodes in acidic media, Science and Technology of Advanced Materials, DOI: [10.1080/14686996.2026.2653417](https://doi.org/10.1080/14686996.2026.2653417)

**To link to this article:** <https://doi.org/10.1080/14686996.2026.2653417>



© 2026 The Author(s). Published by National Institute for Materials Science in partnership with Taylor & Francis Group.



[View supplementary material](#)



Accepted author version posted online: 24 Apr 2026.



[Submit your article to this journal](#)



Article views: 9



[View related articles](#)



[View Crossmark data](#)

**Publisher:** Taylor & Francis & The Author(s). Published by National Institute for Materials Science in partnership with Taylor & Francis Group.

**Journal:** *Science and Technology of Advanced Materials*

**DOI:** 10.1080/14686996.2026.2653417

**Catalyst poisoning influences from various functional groups of energy carriers towards electrochemical oxidation reactions on non-noble high entropy alloy anodes in acidic media**

Rafat Tahawy<sup>a,b</sup>, Salma Aridha Muflihah<sup>a,c,†</sup>, Kosuke Hara<sup>d,†</sup>, Tatsuhiko Ohto<sup>d,\*</sup>, Hisanori Tanimoto<sup>a</sup>, Tianshu Li<sup>a</sup>, Mahmoud Abdelnabi<sup>a,e</sup>, Samuel Jeong<sup>a</sup>, Tomohiko Nishiuchi<sup>f</sup>, Hajime Kimizuka<sup>d</sup>, Akfiny Hasdi Aimon<sup>c,g</sup>, Yoshikazu Ito<sup>a,h,\*</sup>

<sup>a</sup>*Department of Applied Physics, Institute of Pure and Applied Sciences, University of Tsukuba, 1-1-1 Tennodai, Tsukuba, Ibaraki, 305-8573, Japan*

<sup>b</sup>*Central Metallurgical Research and Development Institute (CMRDI), P.O. Box 87 Helwan, 11421, Egypt*

<sup>c</sup>*Department of Physics, Faculty of Mathematics and Natural Sciences, Institut Teknologi Bandung, Bandung, 40132, Indonesia*

<sup>d</sup>*Graduate School of Engineering, Nagoya University, Furo-cho, Chikusa-ku, Nagoya, Aichi 464-8603, Japan*

<sup>e</sup>*Physics Department, Faculty of Science, Ain Shams University, Cairo 11566, Egypt*

<sup>f</sup>*Department of Chemistry, Graduate School of Science, The University of Osaka, 1-1 Machikaneyama, Toyonaka, Osaka 560-0043, Japan*

<sup>g</sup>*Collaboration Research Center for Advanced Energy Materials, National Research and Innovation Agency, Institut Teknologi Bandung, Bandung, 40132, Indonesia*

<sup>h</sup>*Tsukuba Institute for Advanced Research (TIAR), University of Tsukuba, 1-1-1 Tennodai, Tsukuba, Ibaraki, 305-8577, Japan*

**\*Corresponding Author**

Yoshikazu Ito; Email: [ito.yoshikazu.ga@u.tsukuba.ac.jp](mailto:ito.yoshikazu.ga@u.tsukuba.ac.jp)

Tatsuhiko Ohto; Email: [ohito@nagoya-u.jp](mailto:ohito@nagoya-u.jp)

<sup>†</sup>**Equal contribution**

ACCEPTED MANUSCRIPT

# **Catalyst poisoning influences from various functional groups of energy carriers towards electrochemical oxidation reactions on non-noble high entropy alloy anodes in acidic media**

Abstract. Electrolytic synthesis of energy carriers using renewable energy and fuel cells that use energy carriers for regeneration are important technologies for achieving our carbon-neutral society. However, electrochemical reactions in electrolyte containing organic molecules significantly degrades the electrodes by catalyst poisoning (i.e. polymerization of organic molecules on the electrode surface). Such situation can easily occur through the crossover phenomenon between the anode and cathode chambers. Thus, the understanding of the electrochemical reactivity of organic molecules on electrodes becomes important for utilizing energy carriers. This study investigated the electrochemical reactivity of various organic molecules with typical functional groups to understand the reaction mechanism and the subsequent catalyst poisoning in acidic media. While  $\text{-OH}$  groups on organic molecules do not cause significant degradations on a non-noble metal high entropy alloy anode, the coexistence of  $\text{-NH}_2$  and  $\text{C=O}$  groups on organic molecules significantly degrades the anode because the generated polymers block the catalytically active sites. This knowledge will contribute to the effective design of catalysts/electrodes, and benefit the communities in electrolytic synthesis and fuel cells.

Keywords: non-noble metal, high entropy alloy, oxygen evolution reaction, oxidation reaction, anode, catalyst poisoning



## 1. Introduction

Development of green hydrogen technology and fuel cell technologies relevant to energy carriers is a key to utilizing a variety of energy sources in a sustainable carbon neutral society (1-10). Realizing such technologies, diverse energy carriers synthesized by electrolytic synthesis with renewable energy power and several regeneration methods using the energy carriers on fuel cells are necessary. However, impurities such as organic molecules or metal ions in electrolyte often cause severe degradation of the electrodes in electrolysis and fuel cell systems during operation (11,12), which rapidly decrease the electrodes' lifetime (13). Indeed, the development of an international hydrogen supply chain from hydrogen production areas with excess renewable energy to hydrogen consumption areas with limited renewable energy requires hydrogen transportation technology using energy carriers as hydrogen storing materials (i.e. organic chemical hydrides (14-19)). However, the organic chemical hydrides produced at the cathode chamber can cross over from the cathode chamber to the anode chamber through a proton exchange membrane, which causes severe catalyst poisoning on the anodes (16,20-22). Additionally, electrodes in direct methanol fuel cells and another potential fuel cells using chemical fuels containing alcohol (ethanol), aldehyde (formaldehyde), carboxyl (formic acid), and amino (urea) groups are degraded by the crossover of organic molecules from the anode chamber to the cathode chamber (23,24). Therefore, the reactivity of the functional groups of energy carriers with the catalyst must be investigated to reveal the reaction/resistance mechanism toward catalyst poisoning in acidic electrolyte containing simple energy carriers in comparison to the reaction/resistance mechanism using larger organic molecules with several functional groups such as alcohol (glycerol, ethylene glycol), aldehyde (acetaldehyde), carboxyl (lactic acid), and amino (biurea) groups. This will lead to the development of durable

electrodes for use in electrolytic synthesis and fuel cells relevant to energy carriers.

During electrochemical reactions, crossovered organic molecules in electrolyte accompany catalyst poisoning, which could be a major reason of electrode's degradation and prevent the long-term operation of electrolytic synthesis and fuel cells. Catalyst poisoning occurs due to undesirable polymerizations on the surface of electrodes/catalysts, which eventually block the catalytically active sites by the generated polymers (12,16,20). One feasible solution to prevent degradation caused by the crossover of organic molecules is to increase the thickness of the proton exchange membrane (25). However, the crossover cannot be completely prevented due to the diffusion/permeation of organic molecules involved in associated water, pressure differences between an anode and cathode chambers, electroosmosis etc. Another solution is to explore replacements of noble metal catalysts such as Pt and IrO<sub>2</sub> that do not undergo undesirable electrochemical reactions with target organic molecules in acidic environments. Conventional non-noble metal catalysts such as single metal and bimetallic alloys are not actively involved in such electrochemical reactions in comparison to the noble metal catalysts but they are either easily dissolved or completely passivated in acidic media under applied potentials. Thus, a potential candidate can be a non-noble metal-based high-entropy alloy (HEA) electrode because it is known to demonstrate a good balance between catalytic activity and chemical stability during oxidation reactions (i.e. oxygen evolution reaction (OER)) in acidic media (26-38). Additionally, some HEAs decelerate the progress of electrochemical reaction due to the weak adsorption energy of the target organic molecules onto the HEA surface (12). One example is a nonary alloy consisting of Ti, Cr, Mn, Fe, Co, Ni, Zr, Nb, and Mo elements (denoted as 9eHEA). In other words, catalytically inert elements such as passivation elements (for example, Nb) weaken the interaction

between the target organic molecules and the HEA surface compared to the HEA containing catalytically active elements (for example, Ni) and noble metal catalyst such as IrO<sub>2</sub> (12). To design non-noble metal-based anodes that are resistant to catalyst poisoning, influences of organic molecules on catalyst poisoning should be investigated. In particular, the role of functional groups of organic molecules that primarily interact with catalyst surfaces at the adsorption process must be clarified.

This study systematically investigated the electrochemical reactivity and the catalyst poisoning of a non-noble metal-based HEA with the functional groups (for example, alcohol, aldehyde, carboxyl, and amino groups) of energy carriers in an aqueous 0.5 M H<sub>2</sub>SO<sub>4</sub> electrolyte containing an X-molecule such as methanol, ethanol, ethylene glycol, glycerol, acetaldehyde, formaldehyde, formic acid, lactic acid, urea, and biurea. The alcohol, carboxyl and amino groups exhibited strong adsorption energies on the HEA surface and the coexistence of carboxyl and amino groups degrades the anode and the generated polymers block the catalytically active sites on the HEA surface. Furthermore, the degree of catalyst poisoning relevant to the decrease in current density could depend on the characteristics of the functional groups in organic molecules acting as polymer precursors.

## **2. Experimental**

### **2.1 Materials and Synthesis Method**

Button-shaped HEA ingots were produced by arc melting in a pure Ar atmosphere (99.9999%, 60 kPa) (12,39). Each alloy ingot (total weight: 10 g) was synthesized from pure parent metals: Ti (99.9 wt%), Cr (99.99 wt%), Mn (99.99 wt%), Fe (99.95 wt%), Co (99.995 wt%), Ni (99.995 wt%), Zr (99.9 wt%), Nb (99.9 wt%), Mo (99.9 wt%), and

Cu (99.9 wt%), sourced from Hirano Seizaemon Syouten Co., Ltd., Rare Metallic Co., Ltd., Japan Metal Service, Furuuchi Chemical Co., and Materials Research Corp. Before melting the parent metal ingots, a piece of Ti was melted as a typical oxygen trap. Equal molar quantities of nine metals were thoroughly melted, along with the extra addition of Mn (10% equimolar amount), known for its low boiling point and high vapor pressure that causes it to evaporate. Following the total dissolution of the parent metals, the processing and remelting of the ingot were carried out no fewer than six times to synthesize uniformly blended alloys (i.e., homogenization). Then, the resulting ingots were sliced into several sheets using a mechanical slicer and the surface of sliced sheets was polished by sandpapers for characterizations and measurements. In addition, a sliced sheet was mechanically crashed to small particles to observe the elemental distribution at nanoscale.

## 2.2 Characterization

The morphology and microstructure of the synthesized samples were analyzed using scanning electron microscopy (SEM, JEOL JCM-7000 NeoScope), transmission electron microscopy (TEM, JEOL JEM-ARM200F), and energy-dispersive X-ray spectroscopy (EDS; SDD Type, detection surface area 30 mm<sup>2</sup>, solid angle 0.26 sr). X-ray diffraction (XRD) analysis was performed with a D2 PHASER (Cu K $\alpha$ 1 radiation;  $\lambda$  = 1.5406 Å, Bruker). The sample surfaces' organic compounds were analyzed via Fourier-Transform Infrared Spectrometer (FT-IR) spectroscopy (ThermoFisher Nicolet iS50) within the 4000–500 cm<sup>-1</sup> range employing an attenuated total reflectance method. The surface chemical states were analyzed through X-ray photoelectron spectroscopy (XPS; Shimadzu AXIS Ultra DLD) conducted using an Al K $\alpha$  radiation source and an X-ray monochromator. Before the FT-IR, XPS and SEM-EDS measurements, the samples were washed with ethanol after conducting a

chronoamperometry (CA) test for 1 h, and then dried at room temperature. The samples were pasted on a conductive carbon tape for the SEM-EDS measurements and XPS analysis, and the crushed particles were placed on a Cu grid with a carbon support film for TEM measurements.

### 2.3 Electrochemical measurements

Electrochemical tests for the oxygen evolution reaction (OER) in aqueous 0.5 M H<sub>2</sub>SO<sub>4</sub> (pH = 0.5, 95%, Wako) containing X-molecules (X-molecule = methanol (99.8%, Wako), ethanol (99.5%, Wako), urea (99%, Wako), formic acid (88%, Wako), formaldehyde (37%, KANTO Chemical com. Inc.), biurea (Tokyo Chemical Industry Co., LTD.), acetaldehyde (90%, Wako), lactic acid (85-92%, Wako), glycerol (99.5%, Nacalai tesque), ethylene glycol (99.5%, Wako) were conducted in a standard three-electrode electrochemical setup. All experiments were carried out with an electrochemical workstation (Biologic VSP-300) at 25°C under O<sub>2</sub> bubbling (99.9%). The cell was set up with a sat. Ag/AgCl electrode as a reference electrode, a 9eHEA working electrode as an anode, and a graphite rod as a counter electrode. 0.5 M concentration of X-molecules was added into 0.5 M H<sub>2</sub>SO<sub>4</sub> electrolyte. The potentials were referenced to the reversible hydrogen electrode (RHE) through the equation:  $E(\text{RHE}) = E(\text{Ag/AgCl}) + 0.059 \times \text{pH} + 0.197$ . Prior to cyclic voltammetry (CV) measurements, the anodes underwent electrochemical activation through 10 CV cycles within the potential ranges of 0.0–2.2 V (vs. RHE) for HEAs at a scan rate of 5 mV s<sup>-1</sup>. Then, the CV was recorded at a scan rate of 10 mV s<sup>-1</sup>. The double-layer capacitance (C<sub>dl</sub>) was determined from the CV curves obtained at scan rates ranging from 40 to 190 mV s<sup>-1</sup> in the non-Faradaic regions (0.1–0.3 V (vs. RHE) in acidic conditions.

Chronoamperometry (CA) experiments were performed for target current density of 100 mA/cm<sup>2</sup> over 50 h or 1 h for FT-IR measurements. Electrochemical impedance spectroscopy (EIS) tests were conducted at 1.8 V (vs. RHE) with a frequency spectrum of 100  $\mu$ Hz to 1 MHz. Note that same 9eHEA anode (surface area: 0.438 cm<sup>2</sup>) for all CV, C<sub>dl</sub> and EIS measurements was intentionally employed for fair comparisons and the 9eHEA surface was polished before the measurements.

## 2.4 Density Functional Theory (DFT) calculations

DFT calculations were performed with the VASP code (40) using the projected augmented wave method (41) and Perdew-Burke-Ernzerhof as the exchange-correlation function. (42) The plane-wave energy cutoff was set to 400 eV. As the atomic-level structure of 9eHEA is unknown, we adopted a high-throughput protocol with the aid of the machine learning force field (MLFF) using the Gaussian approximated potential (43) and smooth overlap of atomic potential (44) schemes as previously described. (12) The MLFF was constructed from 30 ps-long DFT–MD simulations at 3000 K for a cubic cell (edge length: 15 Å) containing 216 atoms (24 atoms per species). We ran 10 ns classical MD simulations for the same system with the constructed MLFF using the LAMMPS package (45) and selected seven snapshots. Subsequently, we further ran 5-ps DFT–MD simulations and optimized the bulk structures, including the unit cell vectors. Seven surface slab models were created from each bulk structure by inserting a vacuum at  $z = 0, 2, 4, 6, 8, 10$ , and 12 Å, respectively. We obtained 7 (bulk structures)  $\times$  7 (surfaces)  $\times$  2 (upside and downsides of the slab model) = 98 surface models for 9eHEA. To prepare the oxidized surfaces, we added O atoms to all surface atoms of the slab model containing the active site (Ni) with the highest oxygen evolution reaction activity. We employed Grimme's D3(BJ) scheme (46,47) for dispersion correction to

accurately estimate the adsorption energies of glycerol and urea on the oxidized 9eHEA surface.

### 3. Results and discussion

#### 3.1 Material characterizations

A 10 g button-shaped 9eHEA ingots was produced from the pure parent metals using a standard arc melting method. The ingots were sliced into sheets for use as electrodes (**Figure S1**). SEM-EDS measurements confirmed a smooth surface without distinct grain boundaries or elemental segregations (**Figure 1a**). Moreover, high-resolution TEM images of mechanically crushed 9eHEA particles showed crystal lattices (39), while an uniform elemental distribution at the nanoscale was also confirmed by a dark-field scanning transmission electron microscopy (DF-STEM) measurement (**Figure 1b**). XRD spectra of 9eHEA demonstrated the body-centered cubic (*bcc*)-like phase from the four-elemental alloys of Ti, Zr, Nb, and Mo, face-centered cubic (*fcc*) phase from the five-elemental alloys of Cr, Mn, Fe, Co, and Ni, as well as additional phases such as C14 and  $\sigma$  (**Figure S2**) (48,49). These C14 and  $\sigma$  phases could be generated by introducing Ti, Zr, Nb, and Mo into CrMnFeCoNi alloys (50,51). In addition, XPS measurement confirmed that the surface state of 9eHEA was metallic for all elements (**Figure S3**).

### 3.2 Electrochemical OER performances with X-molecules under acidic conditions

Electrochemical OER performance of 9eHEA (with same electrode and same surface which was polished after each measurement) in an aqueous 0.5 M H<sub>2</sub>SO<sub>4</sub> electrolyte, both with and without the X-molecules, was investigated with iR compensation (85%). Note that the oxidation of X-molecules in 0.5 H<sub>2</sub>SO<sub>4</sub> electrolyte does not proceed well without heating and 0.5 M of X-molecules was considered as minimum fuel crossover concentration estimated from the full cell experiments (52) (see more details in supplementary discussion). Cyclic voltammograms were recorded after the CV activation and the balanced performance between catalytic activity and chemical stability, unlike ordinary phenomenon such as either dissolution or complete passivation on non-noble metal catalysts and bimetallic alloy catalysts, was observed. (**Figure 2a** and **Table S1**). 9eHEA in 0.5 M H<sub>2</sub>SO<sub>4</sub> electrolyte with glycerol demonstrated the highest activity whereas 9eHEA in 0.5 M H<sub>2</sub>SO<sub>4</sub> electrolyte with urea demonstrated the lowest activity. The potentials at 100 mA/cm<sup>2</sup> current density of 9eHEA in 0.5 M H<sub>2</sub>SO<sub>4</sub> electrolyte with X-molecules (glycerol, formaldehyde, lactic acid, biurea, methanol acetaldehyde, acetaldehyde) were lower than those without the X-molecules and the potentials at 100 mA/cm<sup>2</sup> current density of 9eHEA in 0.5 M H<sub>2</sub>SO<sub>4</sub> electrolyte with X-molecules (ethanol, formic acid, ethylene glycol, urea) were higher than those without the X-molecules. However, the differences in comparison to the performances without X-molecules were very small except for glycerol and urea (**Figure 2a** and **Table S1**). Indeed, the Tafel slopes of 9eHEA in 0.5 M H<sub>2</sub>SO<sub>4</sub> electrolyte without (126 mV dec<sup>-1</sup>) and with X-molecules (120-134 mV dec<sup>-1</sup>) were quite similar except for urea and biurea (175 and 156 mV dec<sup>-1</sup>) (**Figure 2b** and **Table S1**). In addition, the  $C_{dl}$ , which is almost proportional to the effective electrochemically active surface area



(ECSA), was estimated in a non-Faradaic potential window (0.1–0.3 V vs. RHE) in 0.5 M H<sub>2</sub>SO<sub>4</sub> electrolyte with (21–38 mF/cm<sup>2</sup>) and without X-molecules (22.0 mF/cm<sup>2</sup>) and thereby all  $C_{dl}$  values were quite similar (**Figure S4** and **Table S1**). On the other hand, the electrochemical impedance measurements conducted at 1.8 V (vs. RHE) to estimate the charge-transfer resistance ( $R_{ct}$ ) in 0.5 M H<sub>2</sub>SO<sub>4</sub> electrolyte with and without X-molecules and they demonstrated the large differences (**Figure S5** and **Table S1**). The  $R_{ct}$  values of 9eHEA in 0.5 M H<sub>2</sub>SO<sub>4</sub> electrolyte with X-molecules (450–780 ohm) estimated from an equivalent circuit consisting of a parallel combination with a  $R_{ct}$  and  $C_{dl}$  was lower than that without X-molecules (861 ohm). This indicates that oxidation reactions of X-molecules could occur. The  $R_{ct}$  value of 9eHEA in 0.5 M H<sub>2</sub>SO<sub>4</sub> electrolyte with urea (928 ohm) was higher, which indicated that the oxidation reactions were impeded.

These results showed that ones with similar functional groups demonstrated similar performances and the others with similar functional groups demonstrated different performances. X-molecules with alcohol groups (methanol ethanol, ethylene glycol and glycerol) have similar functional groups. Among these, glycerol, which has the largest number of –OH groups, demonstrated the highest performance. A higher performance with a large number of functional groups was also found in the X-molecules with amino and carboxyl groups (urea and biurea). On the other hand, X-molecules with aldehyde and carboxyl groups (formaldehyde, acetaldehyde, formic acid, lactic acid) have similar functional groups but did not demonstrate significant performance differences. This could be attributed to the quick oxidation of aldehyde groups to carboxyl groups at the oxidation potentials, which is consistent with the electrochemical impedance measurements (**Figure S5** and **Table S1**). Thus, the

electrochemical reactivity depends on the characteristics of the functional groups in organic molecules.

The largest changes were observed on the test with glycerol and urea. Thus, the influence of these substances was further investigated to understand the reaction mechanism. The CA durability of the 9eHEA anodes in 0.5 M H<sub>2</sub>SO<sub>4</sub> electrolyte at ~100 mA/cm<sup>2</sup> current density with glycerol or urea injection (0.5 M concentrations) over 40 h was investigated (**Figure 2c**). The current density dropped after the glycerol injection but the current density gradually recovered and maintained for over 30 h. This durable behavior was also observed in 1000 cycling CV measurement in 0.5 M H<sub>2</sub>SO<sub>4</sub> electrolyte containing glycerol without iR compensation (due to changes over time in the anode's surface state and glycerol concentration in the electrolyte) (**Figure 2d**). Conversely, the current density dropped steeply after the urea injection, but the current density did not recover.

### 3.3 Investigation of catalyst poisoning by X-molecules under acidic conditions

To understand how functional groups affect the catalyst poisoning of 9eHEA, the polymers generated on the surface were investigated by FT-IR spectroscopy after the 1 h CA test in 0.5 M H<sub>2</sub>SO<sub>4</sub> electrolyte containing the X-molecules. Aliphatic hydrocarbon polymer characteristics, such as -CH<sub>2</sub> and -CH<sub>3</sub> stretching vibrations at approximately 2850 and 2919 cm<sup>-1</sup>, as well as the oxidized functional groups (C-O, C=O) were detected on the HEA surface with all X-molecules. This evidence directly supports the formation of polymer (**Figure 3** and **Figure S6-S7**). FT-IR data obtained from the test with X-molecules with alcohol groups (ethanol, ethylene glycol, glycerol) showed an -OH functional group while FT-IR data obtained from the test with X-

molecules with amino groups (urea and biurea) showed a  $\text{-NH}_2$  functional group. However, FT-IR data obtained from the test with X-molecules containing aldehyde and carboxyl groups simply showed the polymer features without  $\text{-OH}$  and  $\text{-NH}_2$  functional groups. Moreover, the surface state of 9eHEA anode after the CA test was investigated with XPS. The XPS detected the polymer characteristics (**Figure S8**). The 9eHEA anode tested with glycerol showed C-C and C-H bonds as well as  $\text{-OH}$  bonds, while the 9eHEA anode tested with urea showed C-C, C-H, C=O and COO bonds as well as C-N and N-H bonds. These suggest that the initial functional groups in glycerol and urea were preserved in the polymer and some of  $\text{-OH}$  and C=O groups in glycerol and urea underwent oxidation. In addition, considering the weak XPS signals of underlaying 9 elements and uniform polymer formation on the surface confirmed by TEM (12), the polymer covers the entire 9eHEA surface.

The SEM-EDS analysis of 9eHEA after the 1 h CA test in 0.5 M  $\text{H}_2\text{SO}_4$  electrolyte with X-molecules revealed large changes in surface morphology after the CA test compared to that before the CA test and without X-molecules (**Figure S9-S19** and **Table S2**). These results suggest that the surface elements were involved in the oxidation reaction with organic molecules (and then the surface elements were probably striped off by X-molecules due to the increase of leaching amount in the existence of organic molecules (**Figure S20**) and the striped atoms could work as polymerization initiators (12). The polymerization occurred during the oxidation reaction, and the generated polymers gradually blocked the catalytically active sites on the HEA surface.

### 3.4 Understanding of adsorption mechanism using DFT calculations

The adsorption energies of the glycerol and urea on the 9eHEA surface were

investigated using DFT calculations to understand the subsequent polymer formation after the adsorption. In our previous report (12,39), the 9eHEA structures were optimized through high-throughput DFT calculations and 2,677 sites on the 9eHEA surface were examined for OER. Accordingly, the most catalytically active sites and catalytically inactive sites were identified as Ni and Nb, respectively, whose active sites could appear on the interface between different phases and glass structure suggested by the analysis with Voronoi tessellation (53) (Figure S21). In addition, Nb was the most electrochemically stable passivation element with highest atomic concentration (Nb: 29.1 at.%) at the 9eHEA surface at OER potential revealed by in situ XPS measurements (39). Thus, Ni and Nb represent the 9eHEA characters and were selected for the target. To simulate the actual situation at oxidation conditions, the optimal surface structure was oxidized for further investigations (Figure 4a and Figure S22).

Single, double and triple  $\text{-OH}$  groups on glycerol were adsorbed on the top of Ni and/or Nb on the surface in an upright direction with the adsorption site of the O from the  $\text{-OH}$  group (Figure 4b-c and Figure S23). In this position, the adsorption of single  $\text{-OH}$  group of glycerol (from  $-1.77$  to  $-1.57$  eV) was weaker than the adsorption of double  $\text{-OH}$  groups of glycerol, and the adsorption of double  $\text{-OH}$  groups of glycerol on the Ni and Nb tops as bridge structures ( $-2.65$  eV) was stronger than that of double  $\text{-OH}$  groups of glycerol on the same Nb top ( $-2.25$  eV). Moreover, as a low probability phenomenon, triple  $\text{-OH}$  groups of glycerol were also strongly adsorbed on the Ni and Nb as bridge structures ( $-2.11$  eV) (Figure 4c and Figure S23). The  $\text{-NH}_2$  and  $\text{C=O}$  groups of urea were adsorbed on the Ni top or Nb top on the surface in an upright or recumbent direction with an adsorption site of N or O from  $\text{CO(NH}_2)_2$  (Figure 4d-g and Figure S24-S25). In the upright and recumbent positions, the adsorption of the  $\text{-NH}_2$  group of urea on the Nb top ( $-1.88$  eV and  $-1.64$  eV) was

weaker than that on the Ni top ( $-2.87$  eV and  $-1.88$  eV). The adsorption of the C=O group of urea was similar to that of  $-\text{NH}_2$  groups of urea on the Nb and Ni tops (from  $-2.82$  to  $-1.83$  eV). This indicates that urea can adsorb onto the surface in any positions. Considering that the passivation element such as Nb significantly contributes to suppress the adsorption of toluene ( $-\text{CH}_3$ ) (from  $-1.30$  to  $-0.36$  eV) and the subsequent polymerization on the 9eHEA surface (12), the adsorption ability of  $-\text{OH}$ ,  $-\text{NH}_2$  and C=O groups on Nb was surely weakened by  $\sim 0.5$  to  $1$  eV compared to Ni. However, Nb does not effectively work to prevent the adsorption and polymerization for glycerol and urea, and thus the  $-\text{OH}$ ,  $-\text{NH}_2$  and C=O groups work as good adsorption sites. In other words, the adsorption of  $-\text{OH}$ ,  $-\text{NH}_2$  and C=O groups is still strong and is considered as chemisorption (54). Indeed, such strong adsorption characteristics rapidly decrease the current density of 9eHEA in electrolyte containing glycerol and, in particular, urea (adsorption energy of  $-2.87$  and  $-2.82$  eV on Ni) strongly blocks the catalytically active Ni sites, further decreasing the current density in electrolyte containing urea compared to that in electrolyte containing glycerol (adsorption energy of  $-1.57$  eV on Ni) (**Figure 2c**).

The difference between glycerol and urea were found in the recovery of current density (**Figure 2c**) and it could be attributed to the size of the molecules, the number of functional groups in the generated polymer and the functional groups' combinations. Since the dipole moments of glycerol and urea were nearly identical ( $3.42 \sim 4.42$  Debye for glycerol, depending on the orientation of OH bonds, and  $3.53$  Debye for urea), the larger molecule (glycerol) experienced greater resistance to movement in  $0.5$  M  $\text{H}_2\text{SO}_4$ , while the smaller molecule (urea) could easily move to the anode surface. Additionally, the generated polymer from urea should have many functional groups, such as  $-\text{NH}_2$  and C=O groups, so that the generated polymers from urea adhere persistently to the

surface anchored by these groups. Thus, the current density decreased and was not recovered (**Figure 2c**). Conversely, the adsorption rate of glycerol to the surface and desorption rate of the generated polymers from glycerol would balance, and thus the current density with glycerol was recovered (**Figure 2c**). This facilitation of desorption of glycerol/polymers is well supported by the DFT result that the adsorption strength of single  $-OH$  group of glycerol (most probable adsorption manner) is much weaker than that of  $-NH_2$  and  $C=O$  groups of urea. Furthermore, since acetaldehyde, formaldehyde, formic acid and lactic acid, which have a single  $C=O$  group with/without a  $-OH$  group(s), do not cause severe degradation on the CV and CA results (**Figure 2a** and **Figure S6**), the coexistence of  $-NH_2$  and  $C=O$  groups could enhance the degradation. Therefore, the adsorption energy of the functional groups and the interplay between the functional groups in the organic molecule and the elements on the surface play an important role in catalyst poisoning.

#### 4. Conclusions

We systematically investigated how various functional groups influence electrochemical reactions and subsequent catalyst poisoning on a non-noble metal high entropy alloy anode in an aqueous 0.5 M  $H_2SO_4$  electrolyte containing methanol, ethanol, ethylene glycol, glycerol, acetaldehyde, formaldehyde, formic acid, lactic acid, urea and biurea. We found that the  $-OH$  groups do not significantly degrade the anode performance, whereas the coexistence of  $-NH_2$  and  $C=O$  groups decrease the anode performance. These differences could be attributed to the coexistence of different functional groups and the nature of the generated polymer which is affected by the target organic molecule acting as polymer precursors. These findings will contribute to

electrolytic synthesis and fuel cells operating with energy carriers for the development of our carbon neutral society.

### **Disclosure statement**

The authors declare that they have no conflicts of interest.

### **Acknowledgement**

We thank Ms. Kazuyo Omura at the Institute for Material Research of Tohoku University for XPS measurements. This work was funded by The Iwatani Naoji Foundation; JSPS Grant-in-Aid for Scientific Research on Innovative Areas ‘High Entropy Alloys’ (Grant Numbers JP19H05166 and JP21H00140); JSPS-Kakenhi (Grant Numbers JP24H00478); Paloma Environmental Technology Development Foundation; JACI Prize for Outstanding Achievements; the Open Facility, Research Facility Center for Science and Technology, University of Tsukuba; the Asahi Grass Foundation; the ENEOS TONENGENERAL Research Foundation; and a cooperative program (Proposal No. 202412-CRKEQ-0009) of the CRDAM-IMR, Tohoku University. R. T. appreciates the Egyptian Cultural Affairs and Missions Sector for his postdoctoral research visit to the University of Tsukuba. M. A. gratefully acknowledges the Matsumae International Foundation (MIF) for supporting his postdoctoral research fellowship (Grant No. 25G08) at the University of Tsukuba. S. A. M. acknowledges the Campus Asia 6 program in University of Tsukuba.

### **References**

- [1] Aricò AS, Bruce P, Scrosati B, et al. Nanostructured materials for advanced energy conversion and storage devices. *Nat Mater.* 2005;4(5):366-377. doi: 10.1038/nmat1368

- [2] Aricò AS, Srinivasan S, Antonucci V. DMFCs: From Fundamental Aspects to Technology Development. *Fuel Cells*. 2001;1(2):133-161. doi: 10.1002/1615-6854(200107)1:2<133::AID-FUCE133>3.0.CO;2-5
- [3] Arsad AZ, Hannan MA, Al-Shetwi AQ, et al. Hydrogen electrolyser technologies and their modelling for sustainable energy production: A comprehensive review and suggestions. *International Journal of Hydrogen Energy*. 2023;48(72):27841-27871. doi: 10.1016/j.ijhydene.2023.04.014
- [4] International Energy Agency. Global Hydrogen Review 2022: IEA; [Available from: <https://www.iea.org/reports/global-hydrogen-review-2022>. ]
- [5] Kojima H, Nagasawa K, Todoroki N, B, et al. Influence of renewable energy power fluctuations on water electrolysis for green hydrogen production. *International Journal of Hydrogen Energy*. 2023;48(12):4572-4593. doi: 10.1016/j.ijhydene.2022.11.018
- [6] Kreuer KD. On the development of proton conducting polymer membranes for hydrogen and methanol fuel cells. *Journal of Membrane Science*. 2001;185(1):29-39. doi: 10.1016/S0376-7388(00)00632-3
- [7] Liu H, Song C, Zhang L, B, et al. A review of anode catalysis in the direct methanol fuel cell. *Journal of Power Sources*. 2006;155(2):95-110. doi: 10.1016/j.jpowsour.2006.01.030
- [8] Shiva Kumar S, Lim H. An overview of water electrolysis technologies for green hydrogen production. *Energy Reports*. 2022;8:13793-13813. doi: 10.1016/j.egyr.2022.10.127
- [9] Wasmus S, Küver A. Methanol oxidation and direct methanol fuel cells: a selective review, *Journal of Electroanalytical Chemistry*. 1999;461(1):14-31. doi: 10.1016/S0022-0728(98)00197-1
- [10] Zhang H, Fu Y, Nguyen HT, et al. Material challenges in green hydrogen ecosystem. *Coordination Chemistry Reviews*. 2023;494:215272. doi: 10.1016/j.ccr.2023.215272
- [11] Casalegno A, Bresciani F, Zago M, Marchesi R. Experimental investigation of methanol crossover evolution during direct methanol fuel cell degradation tests. *Journal of Power Sources*. 2014;249:103-109. doi: 10.1016/j.jpowsour.2013.10.032
- [12] Tajuddin AAH, Ohto T, Tanimoto H, et al. Toluene-Poisoning-Resistant High-Entropy Non-Noble Metal Anode for Direct One-Step Hydrogenation of



- Toluene to Methylcyclohexane. *ChemSusChem*. 2025;18(2):e202401071. doi: 10.1002/cssc.202401071
- [13] Murugan A, Brown AS. Review of purity analysis methods for performing quality assurance of fuel cell hydrogen. *International Journal of Hydrogen Energy*. 2015;40(11):4219-4233. doi: 10.1016/j.ijhydene.2015.01.041
- [14] Izato Y-i, Suzuki T, Iki H, et al. Determining the minimum ignition energy of toluene vapor containing hydrogen towards a risk assessment for liquid organic hydride storage in hydrogen refueling stations. *Fuel*. 2022;310:122236. doi: 10.1016/j.fuel.2021.122236
- [15] Lamb KE, Webb CJ. A quantitative review of slurries for hydrogen storage – Slush hydrogen, and metal and chemical hydrides in carrier liquids. *Journal of Alloys and Compounds*. 2022;906:164235. doi: 10.1016/j.jallcom.2022.164235
- [16] Okada Y, Sasaki E, Watanabe E, et al. Development of dehydrogenation catalyst for hydrogen generation in organic chemical hydride method. *International Journal of Hydrogen Energy*. 2006;31(10):1348-1356. doi: 10.1016/j.ijhydene.2005.11.014
- [17] Shigemasa K, Atienza-Márquez A, Inoue K, et al. Visualization of dragged water and generated hydrogen bubbles in a direct toluene electro-hydrogenation electrolyzer. *Journal of Power Sources*. 2023;554:232304. doi: 10.1016/j.jpowsour.2022.232304
- [18] Shukla A, Karmakar S, Biniwale RB. Hydrogen delivery through liquid organic hydrides: Considerations for a potential technology. *International Journal of Hydrogen Energy*. 2012;37(4):3719-3726. doi: 10.1016/j.ijhydene.2011.04.107
- [19] Wakisaka M, Kunitake M. Direct electrochemical hydrogenation of toluene at Pt electrodes in a microemulsion electrolyte solution. *Electrochemistry Communications*. 2016;64:5-8. doi: 10.1016/j.elecom.2016.01.001
- [20] Amrousse R, Katsumi T, Niboshi Y, et al. Performance and deactivation of Ir-based catalyst during hydroxylammonium nitrate catalytic decomposition. *Applied Catalysis A: General*. 2013;452:64-68. doi: 10.1016/j.apcata.2012.11.038
- [21] Kwan MHT, Pokar NPB, Good C, et al. Deactivation mechanisms of iodo-iridium catalysts in chiral amine racemization. *Tetrahedron*. 2021;80:131823. doi: 10.1016/j.tet.2020.131823

- [22] Wang M, Yue Y, Wang Y, et al. Selective hydrogenation of 1,3-butadiene on iridium nanostructures: Structure sensitivity, host effect, and deactivation mechanism. *Journal of Energy Chemistry*. 2022;69:541-554. doi: 10.1016/j.jechem.2022.01.040
- [23] Ahmed M, Dincer I. A review on methanol crossover in direct methanol fuel cells: challenges and achievements. *International Journal of Energy Research*. 2011;35(14):1213-1228. doi: 10.1002/er.1889
- [24] Gerteisen D. Transient and steady-state analysis of catalyst poisoning and mixed potential formation in direct methanol fuel cells. *Journal of Power Sources*. 2010;195(19):6719-6731. doi: 10.1016/j.jpowsour.2010.04.004
- [25] Nagasawa K, Tanimoto K, Koike J, et al. Toluene permeation through solid polymer electrolyte during toluene direct electro-hydrogenation for energy carrier synthesis. *Journal of Power Sources*. 2019;439:227070. doi: 10.1016/j.jpowsour.2019.227070
- [26] An L, Yang F, Fu C, et al. A Functionally Stable RuMn Electrocatalyst for Oxygen Evolution Reaction in Acid. *Advanced Functional Materials*. 2022;32(27):2200131. doi: 10.1002/adfm.202200131
- [27] Chen C, Xu R, Wang X, et al. Controllable preparation of Ti/TiO<sub>2</sub>-NTs/PbO<sub>2</sub>-CNTs-MnO<sub>2</sub> layered composite materials with excellent electrocatalytic activity for the OER in acidic media. *Ceramics International*. 2021;47(18):25350-25362. doi: 10.1016/j.ceramint.2021.05.257
- [28] Chen X, Xu M, Li S, et al. Ultrafine IrNi Bimetals Encapsulated in Zeolitic Imidazolate Frameworks-Derived Porous N-Doped Carbon for Boosting Oxygen Evolution in Both Alkaline and Acidic Electrolytes. *Advanced Materials Interfaces*. 2020;7(24):2001145. doi: 10.1002/admi.202001145
- [29] Liu K, Zhang C, Sun Y, et al. High-Performance Transition Metal Phosphide Alloy Catalyst for Oxygen Evolution Reaction. *ACS Nano*. 2018;12(1):158-167. doi: 10.1021/acsnano.7b04646
- [30] Lv F, Feng J, Wang K, et al. Iridium-Tungsten Alloy Nanodendrites as pH-Universal Water-Splitting Electrocatalysts. *ACS Central Science*. 2018;4(9):1244-1252. doi: 10.1021/acscentsci.8b00426
- [31] Miles MH, Klaus EA, Gunn BP, et al. The oxygen evolution reaction on platinum, iridium, ruthenium and their alloys at 80°C in acid solutions. *Electrochimica Acta*. 1978;23(6):521-526. doi: 10.1016/0013-4686(78)85030-0

- [32] Pan S, Li H, Liu D, et al. Efficient and stable noble-metal-free catalyst for acidic water oxidation. *Nature Communications*. 2022;13(1):2294. doi: 10.1038/s41467-022-30064-6
- [33] Qiu H-J, Fang G, Gao J, et al. Noble Metal-Free Nanoporous High-Entropy Alloys as Highly Efficient Electrocatalysts for Oxygen Evolution Reaction. *ACS Materials Letters*. 2019;1(5):526-533. doi: 10.1021/acsmaterialslett.9b00414
- [34] Wang F, Kusada K, Wu D, et al. Solid-Solution Alloy Nanoparticles of the Immiscible Iridium–Copper System with a Wide Composition Range for Enhanced Electrocatalytic Applications. *Angewandte Chemie International Edition*. 2018;57(17):4505-4509. doi: 10.1002/anie.201800650
- [35] Wang Y, Zhang L, Yin K, et al. Nanoporous Iridium-Based Alloy Nanowires as Highly Efficient Electrocatalysts Toward Acidic Oxygen Evolution Reaction. *ACS Applied Materials & Interfaces*. 2019;11(43):39728-39736. doi: 10.1021/acsami.9b09412
- [36] Wang Z, Zheng Y-R, Chorkendorff I, et al. Acid-Stable Oxides for Oxygen Electrocatalysis. *ACS Energy Letters*. 2020;5(9):2905-2908. doi: 10.1021/acsenenergylett.0c01625
- [37] Zhang D, Shi Y, Chen X, et al. High-entropy alloy metallene for highly efficient overall water splitting in acidic media. *Chinese Journal of Catalysis*. 2023;45:174-183. doi: 0.1016/S1872-2067(22)64166-4
- [38] Zhou L, Liu X, Wang K, et al. One-Pot Synthesis of Alloy Ir–Cu Microspheres with Excellent Electro-Catalytic Activity Toward Oxygen Evolution Reaction under Acidic Conditions. *Energy & Fuels*. 2020;34(8):9956-9962. doi: 10.1021/acs.energyfuels.0c01581
- [39] Tajuddin AAH, Wakisaka M, Ohto T, et al. Corrosion-Resistant and High-Entropic Non-Noble-Metal Electrodes for Oxygen Evolution in Acidic Media. *Advanced Materials*. 2023;35(3):2207466. doi: 10.1002/adma.202207466
- [40] Kresse G, J. Hafner J. Norm-conserving and ultrasoft pseudopotentials for first-row and transition elements. *J. Phys. Condens. Matter*. 1994;6:8245. doi: 10.1088/0953-8984/6/40/015
- [41] Blöchl PE. Projector augmented-wave method. *Phys. Rev. B*. 1994;50:17653. doi: 10.1103/PhysRevB.50.17953
- [42] Perdew JP, Burke K, Ernzerhof M. Generalized Gradient Approximation Made Simple *Phys. Rev. Lett*. 1997;77:3865. doi: 10.1103/PhysRevLett.77.3865

- [43] Bartók AP, Payne MC, Kondor R, Csányi G. Gaussian Approximation Potentials: The Accuracy of Quantum Mechanics, without the Electrons. *Phys. Rev. Lett.* 2010;104:136403. doi: 10.1103/PhysRevLett.104.136403
- [44] Bartók AP, Kondor R, Csányi G. On representing chemical environments. *Phys. Rev. B.* 2013;87:184115. doi: 10.1103/PhysRevB.87.184115
- [45] Thompson AP, Aktulga HM, Berger R, et al. LAMMPS - a flexible simulation tool for particle-based materials modeling at the atomic, meso, and continuum scales. *Comput. Phys. Commun.* 2022;271:108171. doi: 10.1016/j.cpc.2021.108171
- [46] Grimme S, Antony J, Ehrlich S, et al. A consistent and accurate ab initio parametrization of density functional dispersion correction (DFT-D) for the 94 elements H-Pu. *J. Chem. Phys.* 2010;132:154104. doi: 10.1063/1.3382344
- [47] Grimme S, Ehrlich S, Goerigk L. Effect of the damping function in dispersion corrected density functional theory *J. Comput. Chem.* 2011;32:1456. doi: 10.1002/jcc.21759
- [48] Karantzalis AE, Poulia A, Kamnis S, et al. Modification of Cantor High Entropy Alloy by the Addition of Mo and Nb: Microstructure Evaluation, Nanoindentation-Based Mechanical Properties, and Sliding Wear Response Assessment. *Alloys.* 2022;1:70. doi: 10.3390/alloys1010006
- [49] Tsai M-H, Chang K-C, Li J-H, et al. A second criterion for sigma phase formation in high-entropy alloys. *Materials Research Letters.* 2016;4(2):90-95. doi: 10.1080/21663831.2015.1121168
- [50] Krapivka MO, Myslyvchenko OM, Karpets MV. Base Alloy Concept in the Development of High-Entropy Materials. *Powder Metall. Metal. Ceram.* 2018;56:589. doi: 10.1007/s11106-018-9932-x
- [51] Edalati P. Reversible room temperature hydrogen storage in high-entropy alloy TiZrCrMnFeNi. *Scripta materialia.* 2020;178:387-390. doi: 10.1016/j.scriptamat.2019.12.009
- [52] Jeong KJ, Miesse CM, Choi JH, et al. Fuel crossover in direct formic acid fuel cells, *Journal of Power Sources.* 2027;168:119–125. doi: 10.1016/j.jpowsour.2007.02.062
- [53] Zhou W, Song J, Lin L, et al, npj Computational Materials, 2025;11:69. doi: 10.1038/s41524-025-01561-1

- [54] Araujo RB, Rodrigues GLS, Santos EC, et al. Adsorption energies on transition metal surfaces: towards an accurate and balanced description. *Nature Communications*. 2022;13:6853 doi: 10.1038/s41467-022-34507-y

ACCEPTED MANUSCRIPT

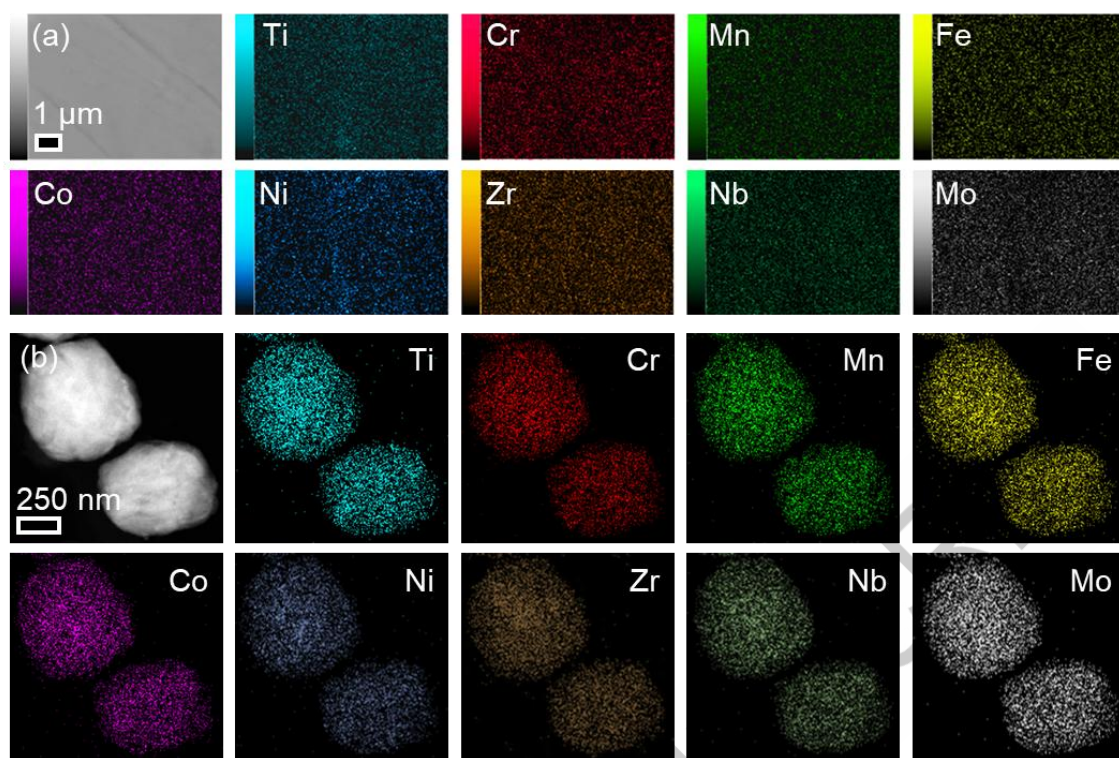


Figure 1. (a) SEM-EDS mapping and (b) STEM-EDS mapping of 9eHEA. Scale bars were 1  $\mu\text{m}$  and 250 nm, respectively.

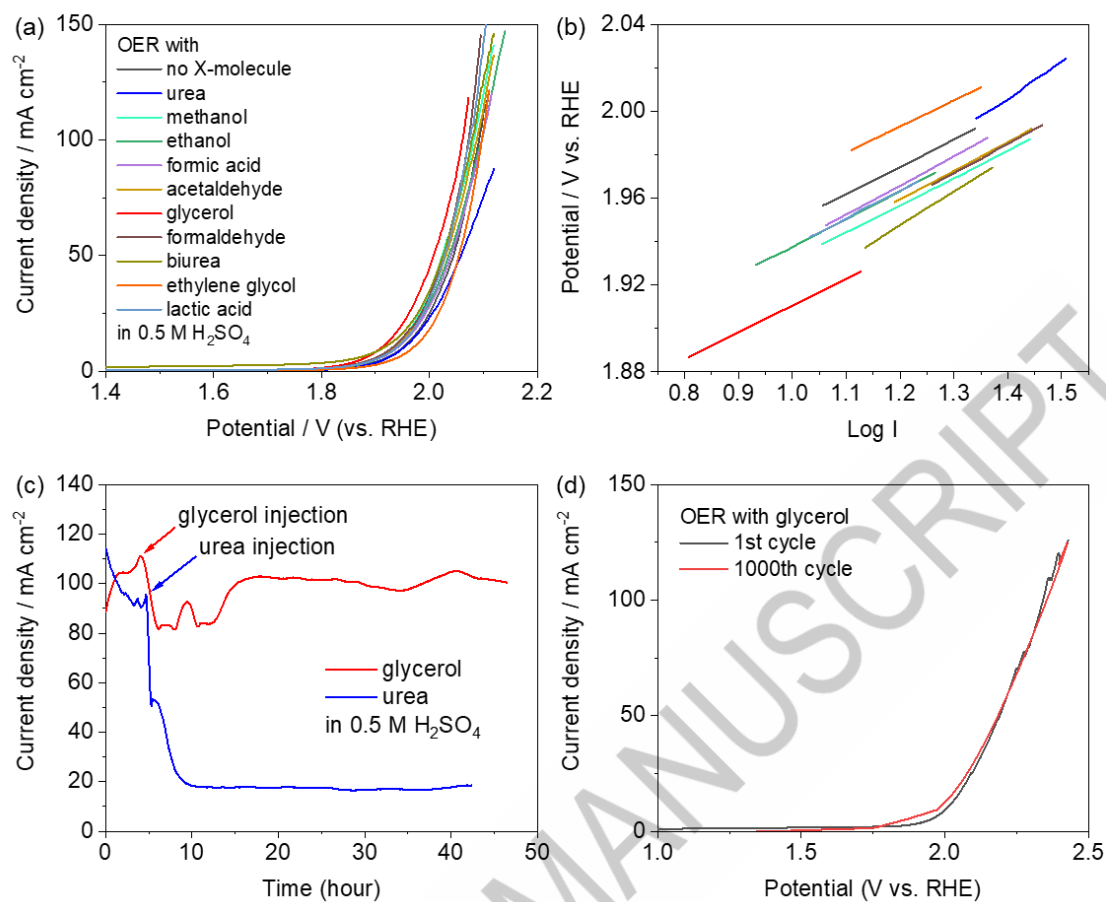


Figure 2. (a) CV measurements and (b) the Tafel slope of 9eHEA anode in aqueous 0.5 M H<sub>2</sub>SO<sub>4</sub> electrolyte containing X-molecules or without X-molecule. (c) CA measurements of 9eHEA anode in aqueous 0.5 M H<sub>2</sub>SO<sub>4</sub> electrolyte with the glycerol and urea injection. (d) Cycling stability test of 9eHEA anode in aqueous 0.5 M H<sub>2</sub>SO<sub>4</sub> electrolyte containing glycerol.

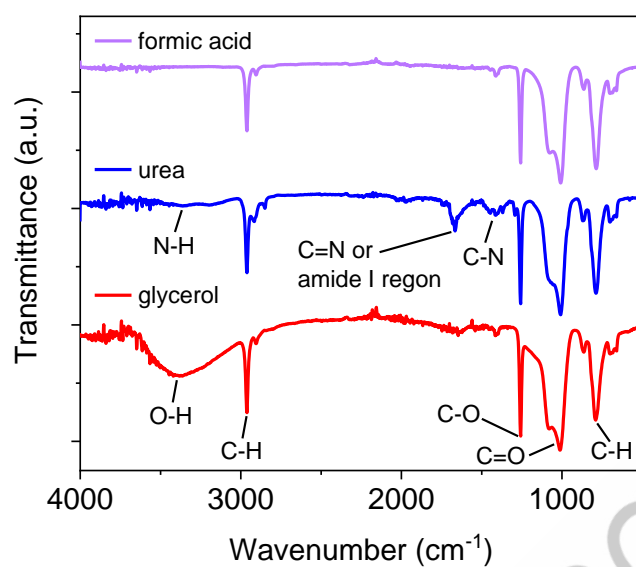


Figure 3. FT-IR results on the surface of 9eHEA anode tested in aqueous 0.5 M H<sub>2</sub>SO<sub>4</sub> electrolyte containing formic acid, urea and glycerol from 1 h CA measurements.



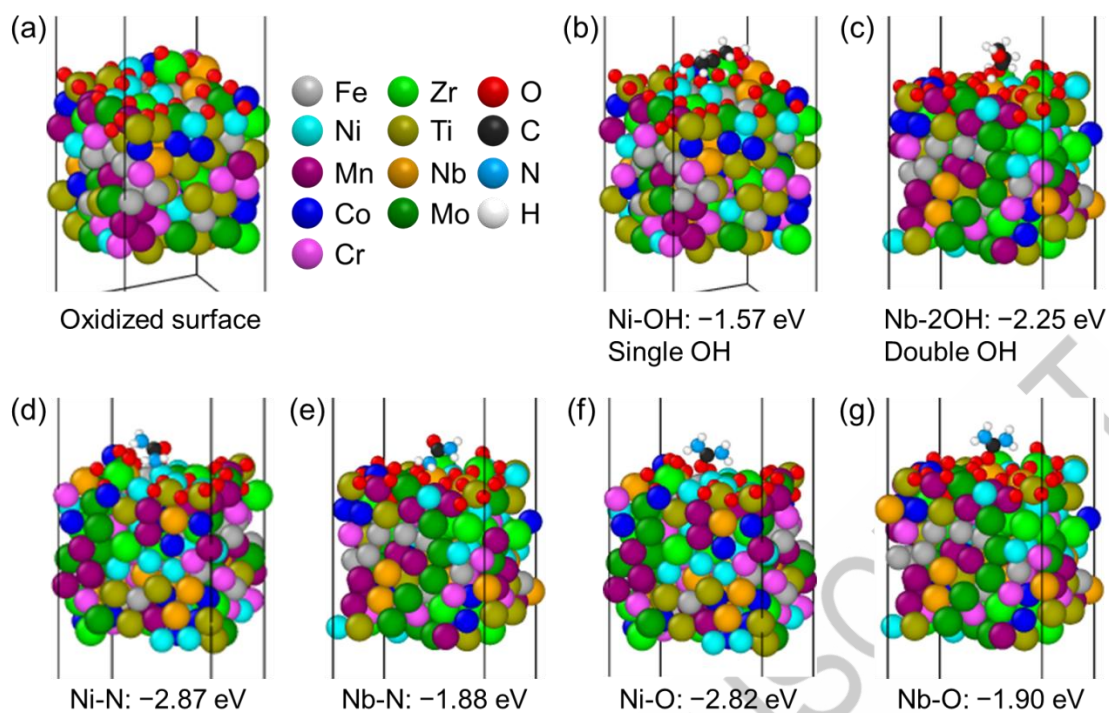
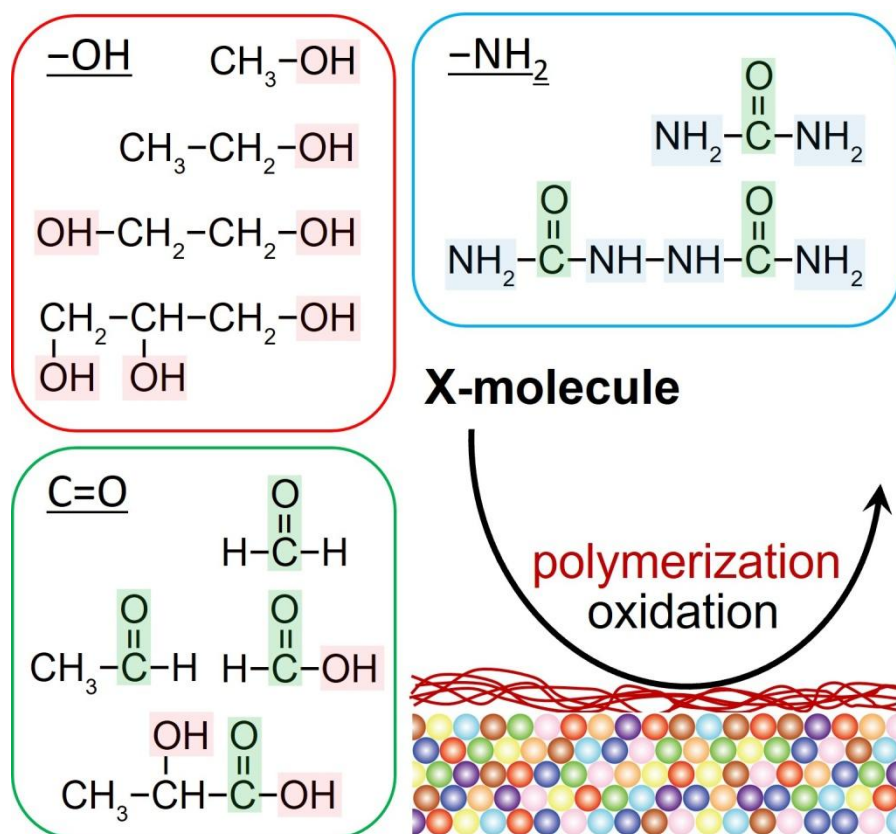


Figure 4. DFT calculations of glycerol and urea adsorption on an oxidized 9eHEA model. (a) Oxidized surface model with color codes of elements. (b) Single -OH adsorption on Ni, (c) double -OH adsorption on same Nb, (d) -NH<sub>2</sub> adsorption on Ni, (e) -NH<sub>2</sub> adsorption on Nb, (f) C=O adsorption on Ni, (g) C=O adsorption on Nb.

Graphical Abstract



## Supplementary material

### Catalyst poisoning influences from various functional groups of energy carriers towards electrochemical oxidation reactions on non-noble high entropy alloy anodes in acidic media

Rafat Tahawy<sup>a,b</sup>, Salma Aridha Muflihah<sup>a,c,†</sup>, Kosuke Hara<sup>d,†</sup>, Tatsuhiko Ohto<sup>d,\*</sup>, Hisanori Tanimoto<sup>a</sup>, Tianshu Li<sup>a</sup>, Mahmoud Abdelnabi<sup>a,e</sup>, Samuel Jeong<sup>a</sup>, Tomohiko Nishiuchi<sup>f</sup>, Hajime Kimizuka<sup>d</sup>, Akfiny Hasdi Aimon<sup>c,g</sup>, Yoshikazu Ito<sup>a,h,\*</sup>

<sup>a</sup>*Department of Applied Physics, Institute of Pure and Applied Sciences, University of Tsukuba, 1-1-1 Tennodai, Tsukuba, Ibaraki, 305-8573, Japan*

<sup>b</sup>*Central Metallurgical Research and Development Institute (CMRDI), P.O. Box 87 Helwan, 11421, Egypt*

<sup>c</sup>*Department of Physics, Faculty of Mathematics and Natural Sciences, Institut Teknologi Bandung, Bandung, 40132, Indonesia*

<sup>d</sup>*Graduate School of Engineering, Nagoya University, Furo-cho, Chikusa-ku, Nagoya, Aichi 464-8603, Japan*

<sup>e</sup>*Physics Department, Faculty of Science, Ain Shams University, Cairo 11566, Egypt*

<sup>f</sup>*Department of Chemistry, Graduate School of Science, The University of Osaka, 1-1 Machikaneyama, Toyonaka, Osaka 560-0043, Japan*

<sup>g</sup>*Collaboration Research Center for Advanced Energy Materials, National Research and Innovation Agency, Institut Teknologi Bandung, Bandung, 40132, Indonesia*

<sup>h</sup>*Tsukuba Institute for Advanced Research (TIAR), University of Tsukuba, 1-1-1 Tennodai, Tsukuba, Ibaraki, 305-8577, Japan*

**\*Corresponding Author**

Yoshikazu Ito; Email: [ito.yoshikazu.ga@u.tsukuba.ac.jp](mailto:ito.yoshikazu.ga@u.tsukuba.ac.jp)

Tatsuhiko Ohto; Email: [ohito@nagoya-u.jp](mailto:ohito@nagoya-u.jp)

**†Equal contribution**

## Supplementary discussion

Our research target is the concentrations of crossover molecules in the counter chamber and the target concentrations of X-molecule were roughly estimated by the crossover flux quantity using the report [S1].

The crossover current density ( $j_{crossover}$ ) was estimated by

$$j_{crossover} = M_{fuel} N_e F$$

where  $M_{fuel}$  is the molar flux of fuel crossover (based on a CO<sub>2</sub> detector signal),  $N_e$  is the number of electrons per molecule of fuel that are transferred in the fuel cell's preferred electrochemical reaction, and  $F$  is the Faraday constant. For formic acid and methanol, the values of  $N_e$  are 2 and 6, respectively. Thus, the  $M_{fuel}$  can be estimated when we determine the  $j_{crossover}$  with gas chromatography method for detecting CO<sub>2</sub> emitted from the fuel cell. Assuming that the volume containing crossovered molecules at the cathode side (i.e. an intentionally overestimated 0.1 cm thickness water layer from Nafion membrane) is 0.1 mL per MEA area (cm<sup>2</sup>), the estimated crossover molar concentrations of fuel molecules between the Nafion membrane (cathode side) and carbon paper (facing to the Nafion) exceed 0.5 M (see the table). Thus, we set the 0.5 M concentration for initial understanding of crossover characters of X-molecules in our manuscript.

Crossover current	$M_{fuel}$ (mmol/cm <sup>2</sup> /h)	Fuel concentration (mol/L) after 1 hour operation near the Nafion membrane
10 mA/cm <sup>2</sup> formic acid	0.187	1.87 M
10 mA/cm <sup>2</sup> methanol	0.062	0.62 M
10 mA/cm <sup>2</sup> formic acid	1.87	18.7 M
10 mA/cm <sup>2</sup> methanol	0.62	6.2 M

ACCEPTED MANUSCRIPT

## Supplementary Figures

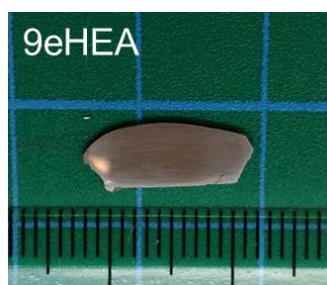


Figure S1. A photograph of a 9eHEA sheet.

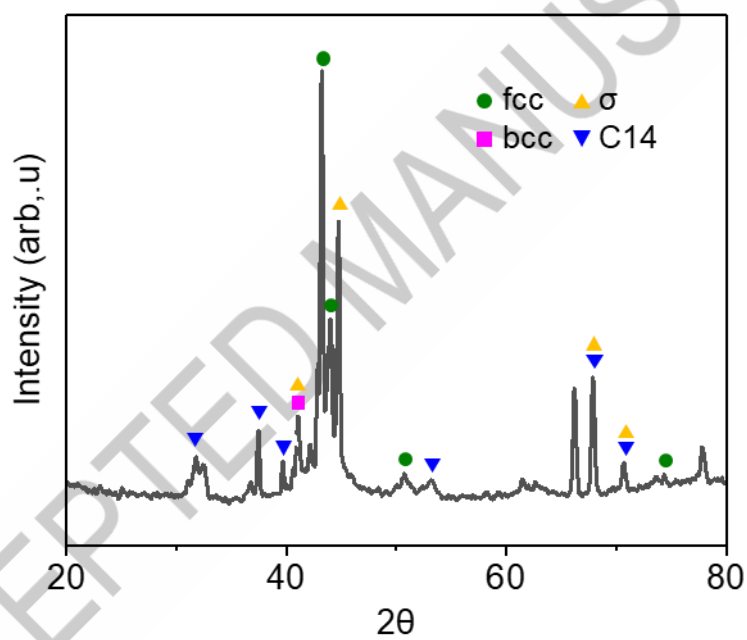


Figure S2. XRD spectra of 9eHEA sheet.

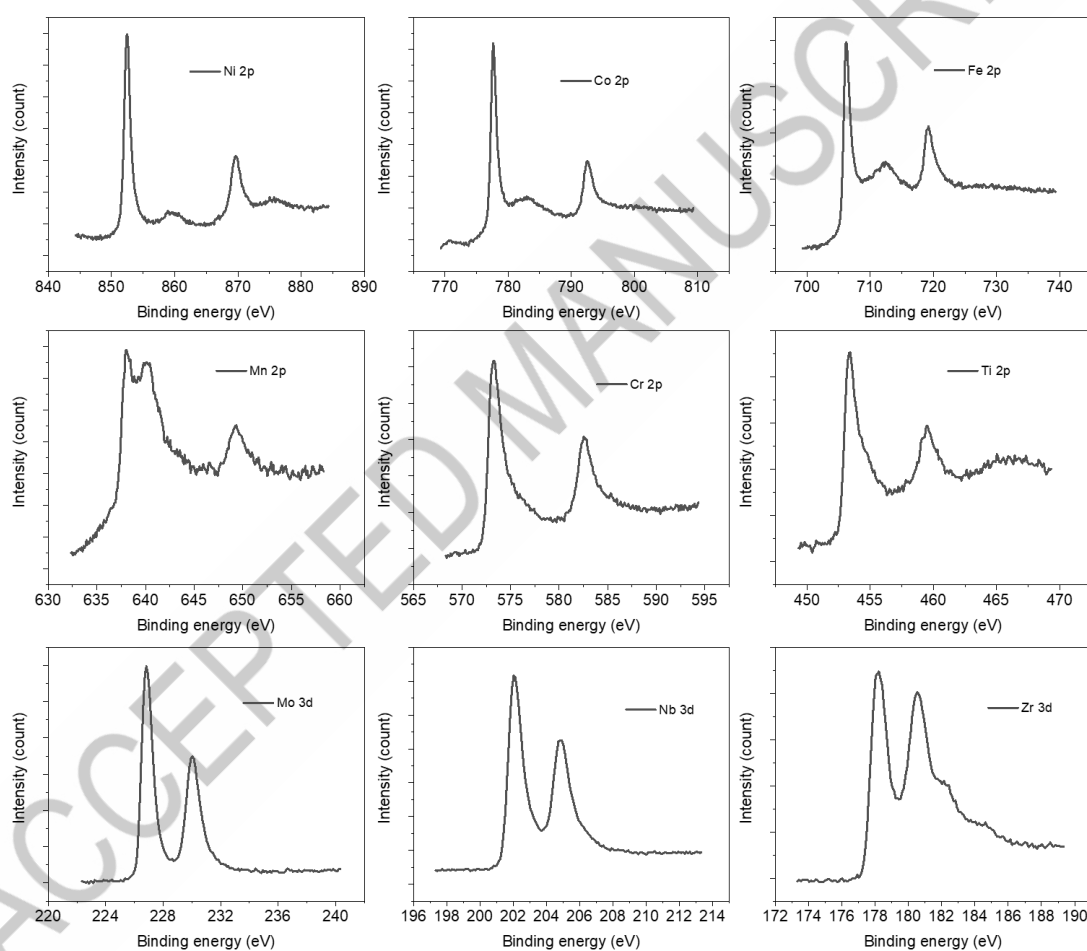
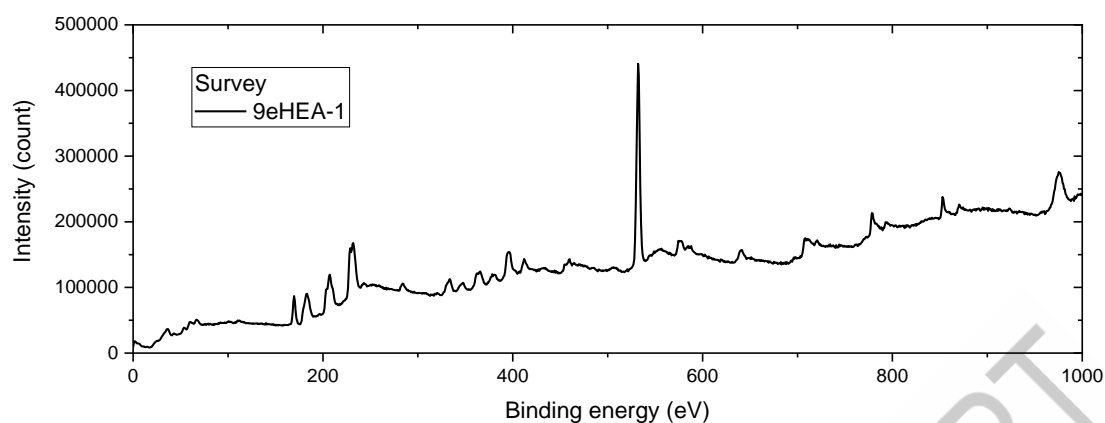


Figure S3. XPS spectra of as-prepared 9eHEA sheet. Some of metals were oxidized under air.

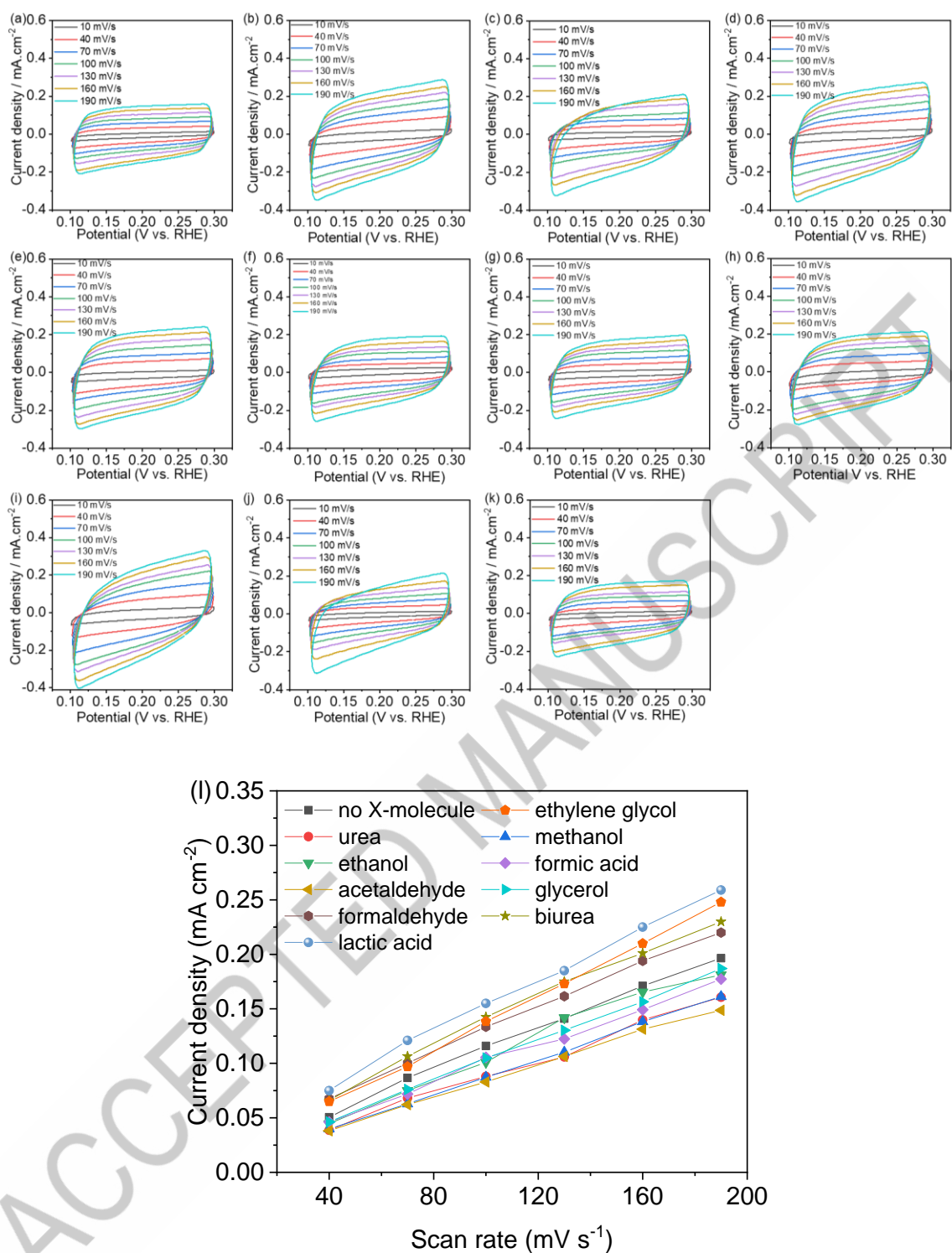


Figure S4. Cyclic voltammogram of 9eHEA anode in non-faradaic region of X-molecules such as (a) acetaldehyde, (b) biurea, (c) ethanol, (d) ethylene glycol, (e) formaldehyde, (f) formic acid, (g) glycerol, (h) no X-molecules, (i) lactic acid, (j) methanol and (k) urea with (l) the plot.



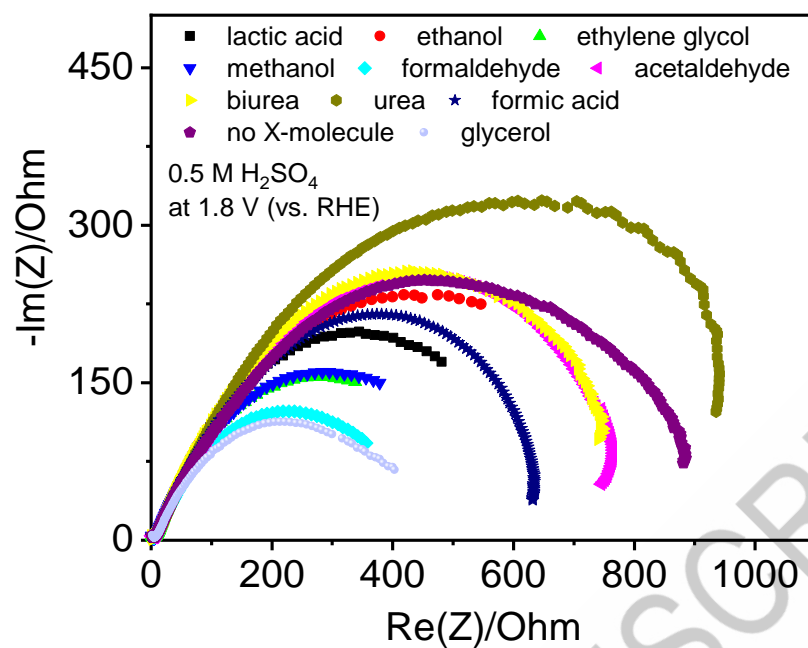


Figure S5. Electrochemical impedance spectroscopy of 9eHEA anode in 0.5 M H<sub>2</sub>SO<sub>4</sub> electrolyte containing X-molecules or no X-molecule.

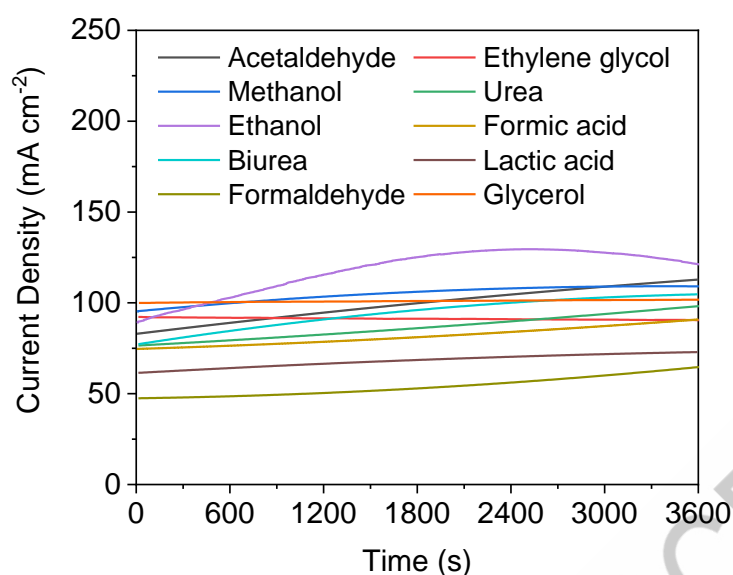


Figure S6. 1 h CA measurements of 9eHEA anode in 0.5 M  $\text{H}_2\text{SO}_4$  electrolyte containing X-molecules for FT-IR measurements. The current density trends in Figure S6 were not matched with those in Figure 2(a) due to the use of different 9eHEA batch samples (the sample in Figure 2(a) was broken during FT-IR setup so that the different batch samples were employed for Figure S6).

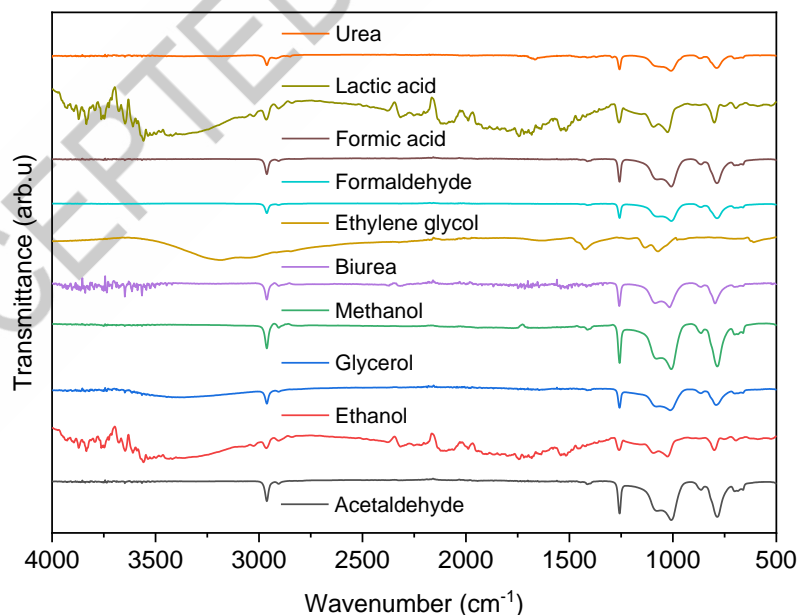


Figure S7. FT-IR results on the surface of 9eHEA anode tested in 0.5 M  $\text{H}_2\text{SO}_4$  electrolyte containing X-molecules from 1 h CA measurements.

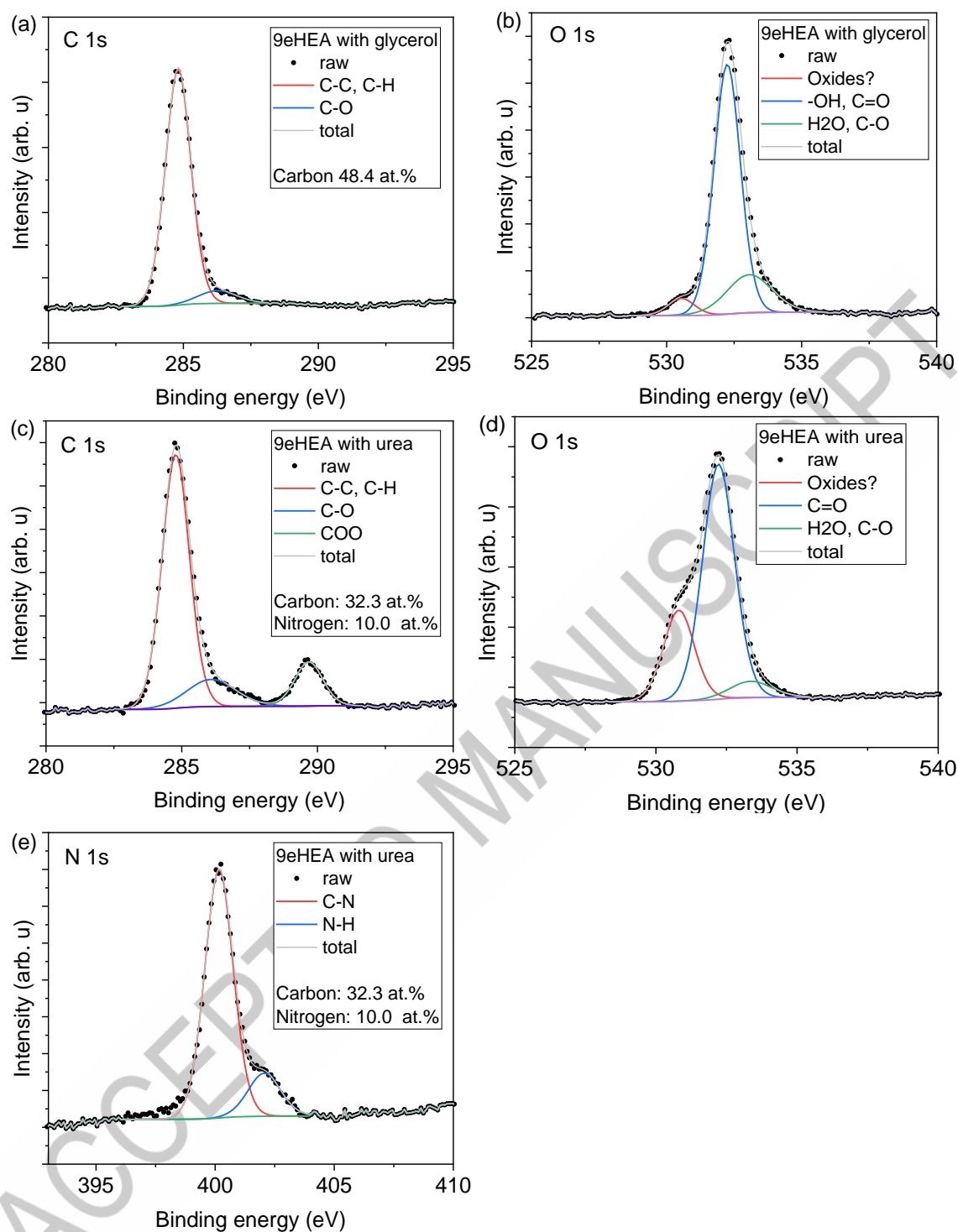


Figure S8. XPS spectra of 9eHEA sheet after the CA test with (a-b) glycerol (C: 48.4 at.%, O: 29.1 at.% in total) and (c-e) urea (C: 32.3 at.%, O: 39.0 at.%, N: 10.0 at.% in total). The 9eHEA elements were not clearly detected due to the polymer influences.

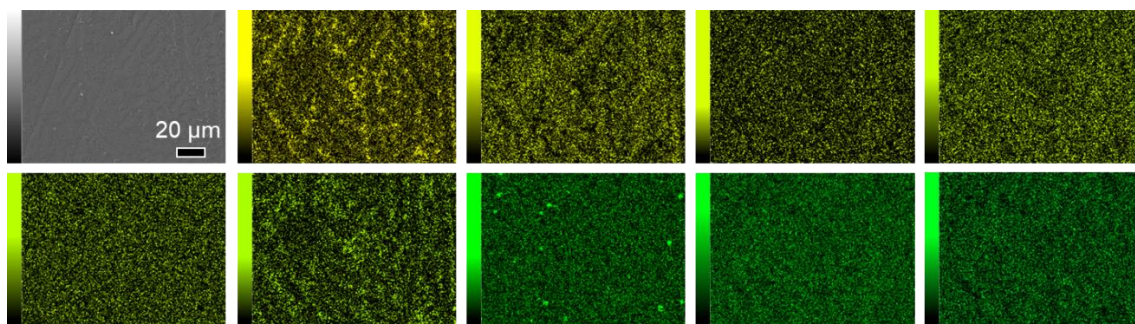


Figure S9. SEM-EDS mapping of the surface of 9eHEA anode tested in 0.5 M  $\text{H}_2\text{SO}_4$  electrolyte without X-molecule from 1 h CA measurements.

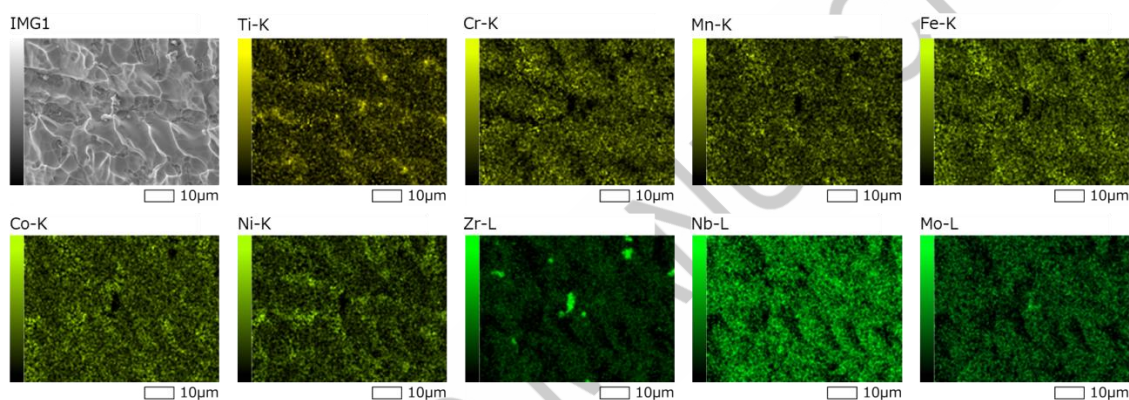


Figure S10. SEM-EDS mapping of the surface of 9eHEA anode tested in 0.5 M  $\text{H}_2\text{SO}_4$  electrolyte containing acetaldehyde from 1 h CA measurements.

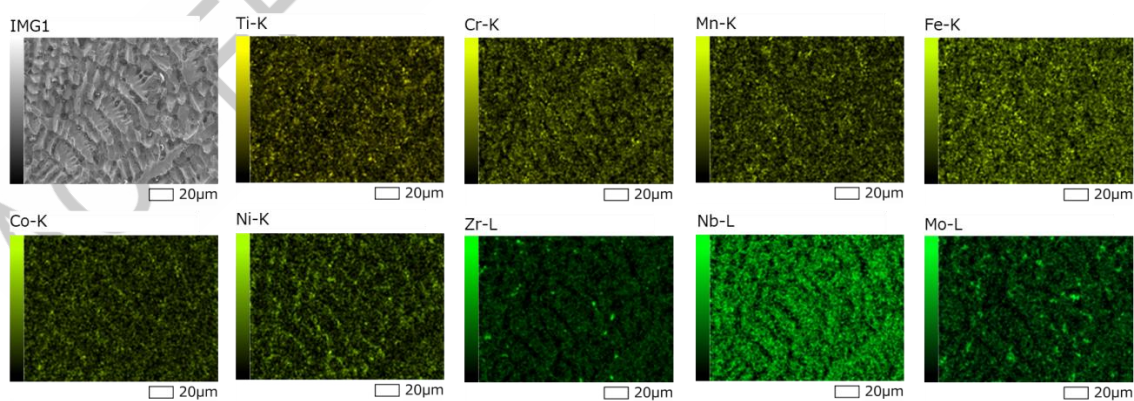


Figure S11. SEM-EDS mapping of the surface of 9eHEA anode tested in 0.5 M  $\text{H}_2\text{SO}_4$  electrolyte containing biurea from 1 h CA measurements.



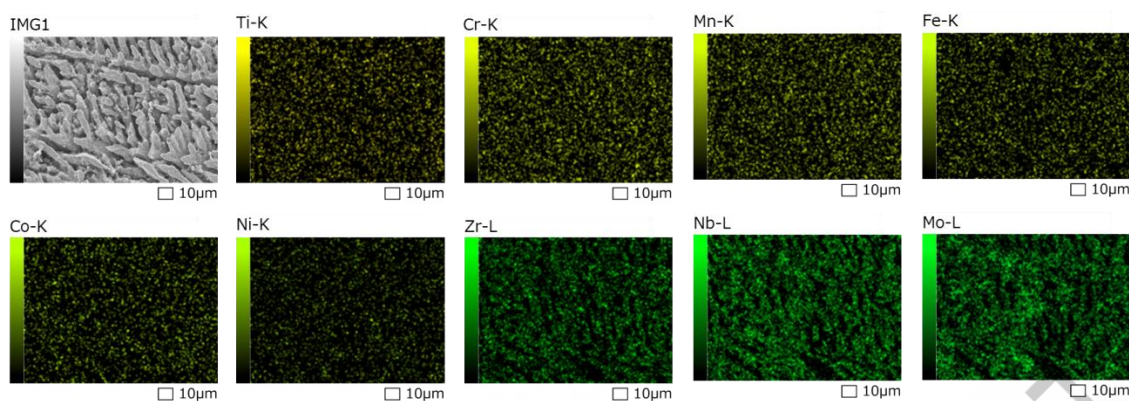


Figure S12. SEM-EDS mapping of the surface of 9eHEA anode tested in 0.5 M  $\text{H}_2\text{SO}_4$  electrolyte containing ethylene glycol from 1 h CA measurements.

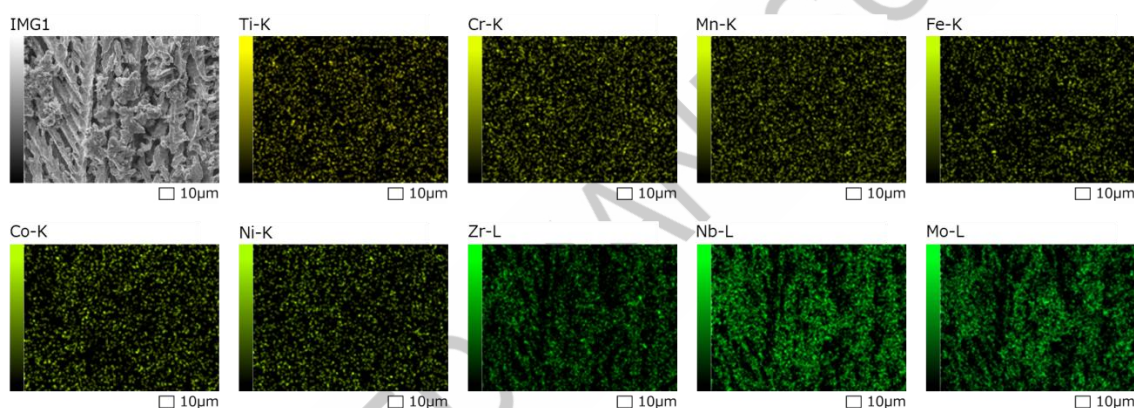


Figure S13. SEM-EDS mapping of the surface of 9eHEA anode tested in 0.5 M  $\text{H}_2\text{SO}_4$  electrolyte containing ethanol from 1 h CA measurements.

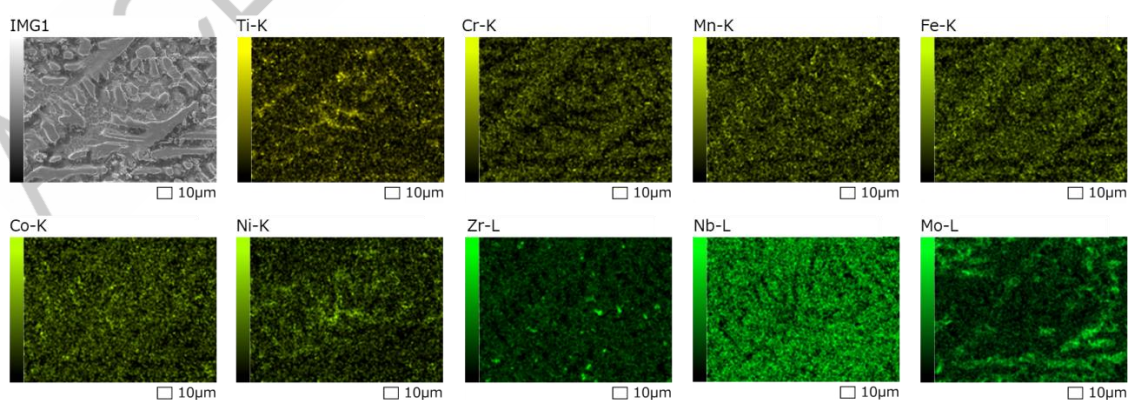


Figure S14. SEM-EDS mapping of the surface of 9eHEA anode tested in 0.5 M  $\text{H}_2\text{SO}_4$  electrolyte containing formaldehyde from 1 h CA measurements.

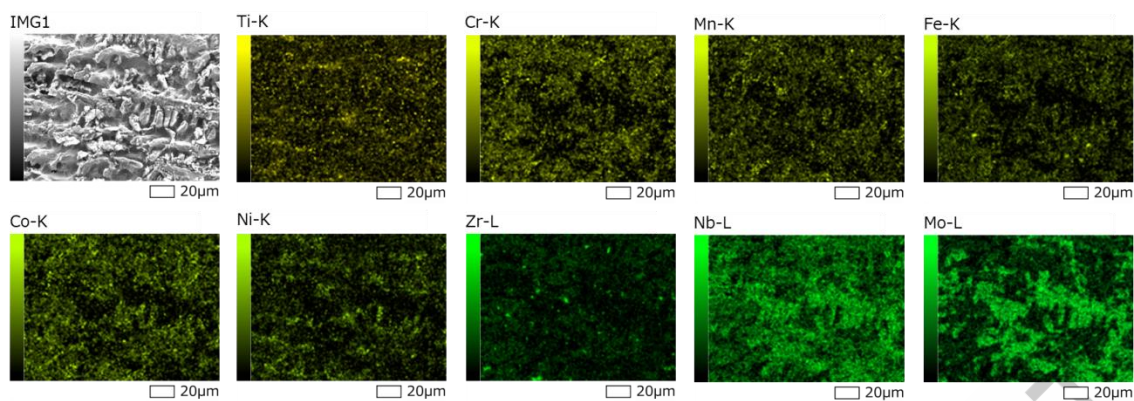


Figure S15. SEM-EDS mapping of the surface of 9eHEA anode tested in 0.5 M  $\text{H}_2\text{SO}_4$  electrolyte containing formic acid from 1 h CA measurements.

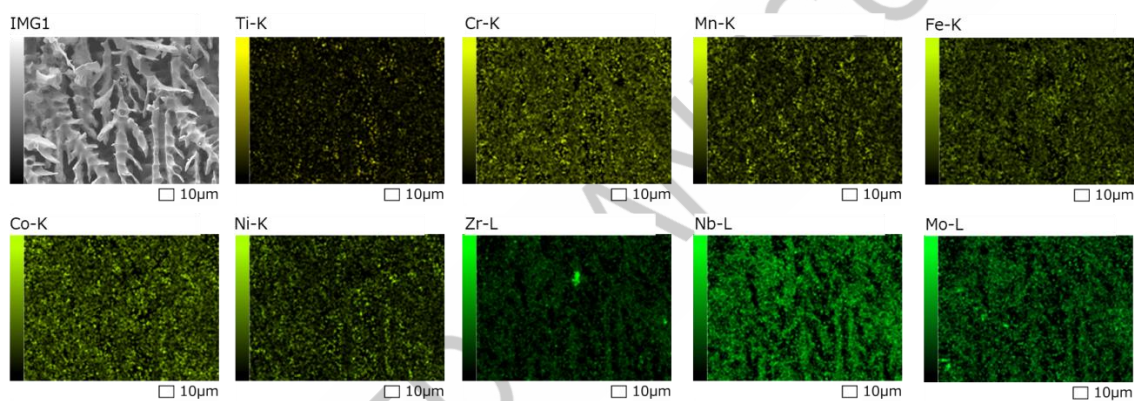


Figure S16. SEM-EDS mapping of the surface of 9eHEA anode tested in 0.5 M  $\text{H}_2\text{SO}_4$  electrolyte containing glycerol from 1 h CA measurements.

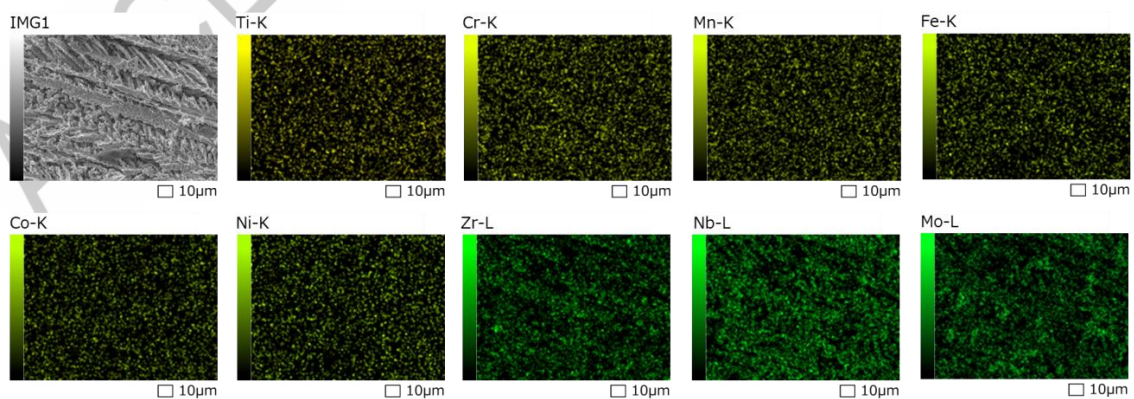


Figure S17. SEM-EDS mapping of the surface of 9eHEA anode tested in 0.5 M  $\text{H}_2\text{SO}_4$  electrolyte containing methanol from 1 h CA measurements.



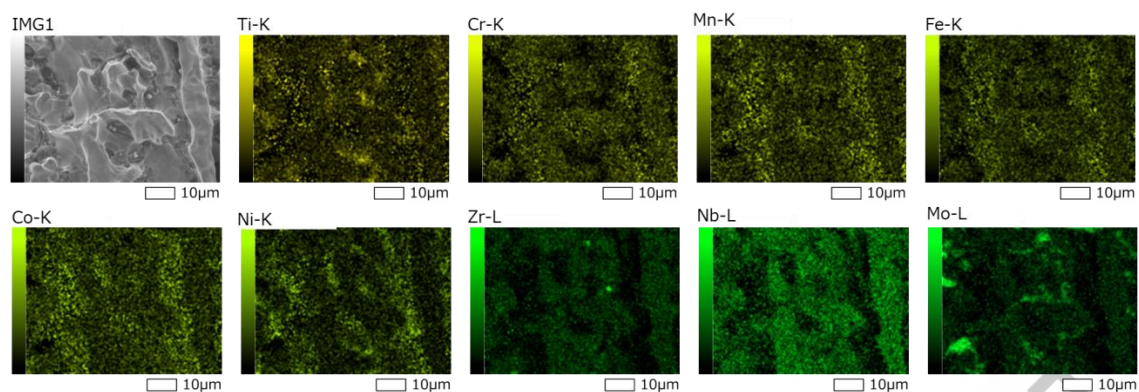


Figure S18. SEM-EDS mapping of the surface of 9eHEA anode tested in 0.5 M  $\text{H}_2\text{SO}_4$  electrolyte containing lactic acid from 1 h CA measurements.

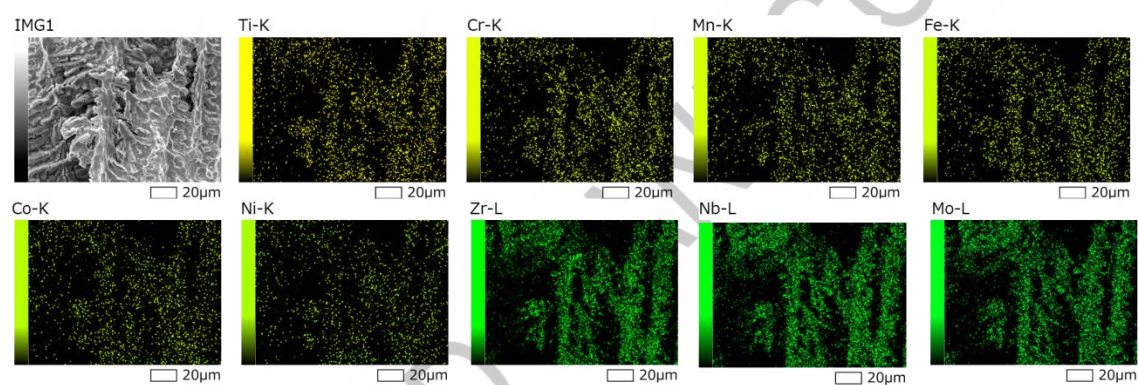


Figure S19. SEM-EDS mapping of the surface of 9eHEA anode tested in 0.5 M  $\text{H}_2\text{SO}_4$  electrolyte containing urea from 1 h CA measurements.

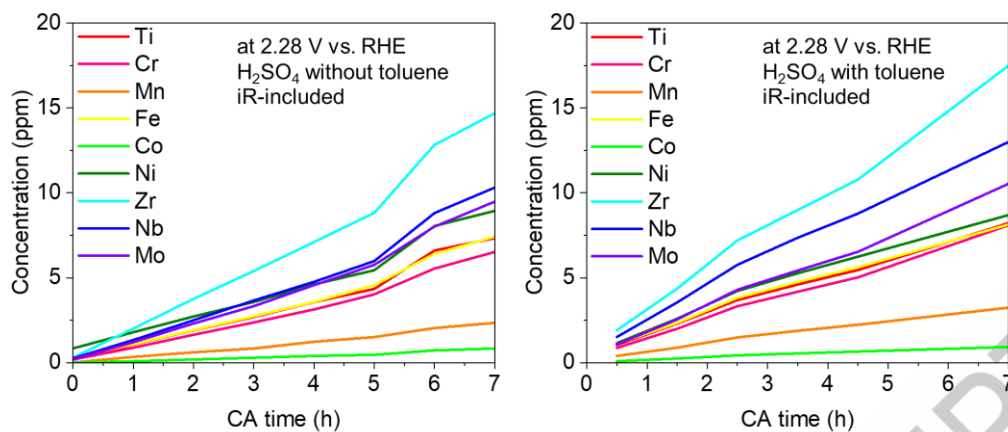


Figure S20. ICP-OES analysis of electrolyte in anode from the CA test with and without toluene. The leaching amount increased by 5-15% in the existence of toluene [S2].



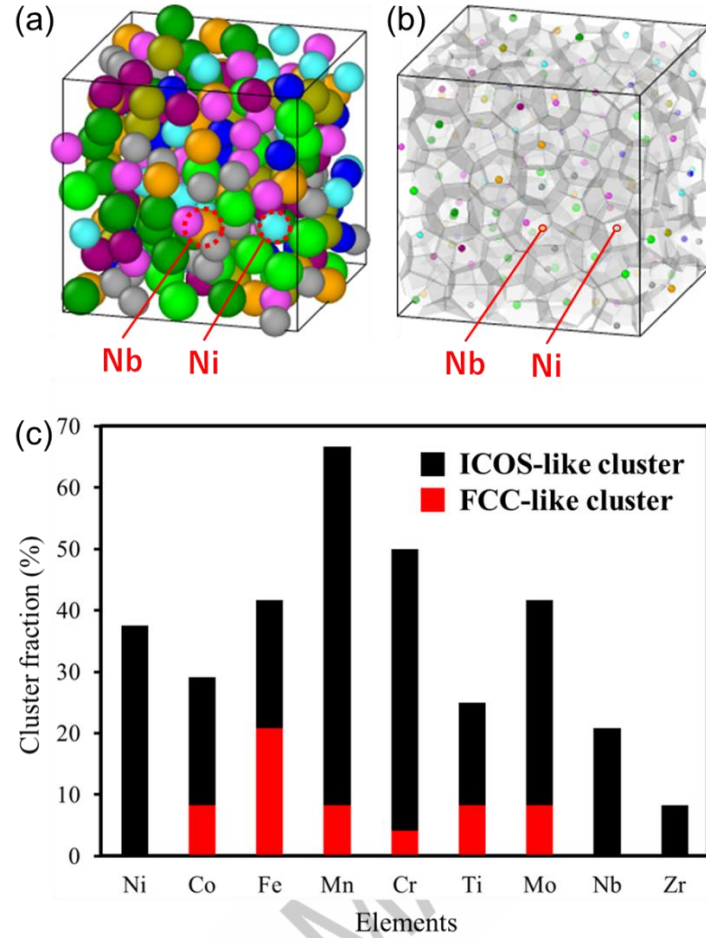


Figure S21. Voronoi tessellation. (a) Bulk structures of 9eHEA just before cutting the surface. Ni and Nb considered as active sites were indicated. (b) Voronoi tessellation of (a). (c) Fraction of the clusters for each atom. To investigate the local atomic environments of the active sites, we additionally performed the Voronoi tessellation for the bulk system just before cutting the surface [S3]. The bulk system in (a) was one of the structures annealed from 3000 K with the aid of machine-learning force field as previously reported [S4], whose simulated annealing processes can simulate as many phases appeared in the real crystal as possible. A Voronoi polyhedron is defined by Schläfli's notation,  $\langle n_3, n_4, n_5, n_6 \rangle$ , where  $n_i$  is the number of  $i$ -edged faces of a polyhedron. The Voronoi indices of standard BCC, FCC, and icosahedral (ICOS) are  $\langle 0, 6, 0, 8 \rangle$ ,  $\langle 0, 12, 0, 0 \rangle$ , and  $\langle 0, 0, 12, 0 \rangle$ , respectively [S3]. The cluster consists of FCC and ICOS, while BCC (not shown here) also exists in other six bulk structures in our calculations. The target Ni and Nb were mainly involved in ICOS. This indicates that the active sites exist in other phases except BCC and FCC, or the interface between phases and glass structure.

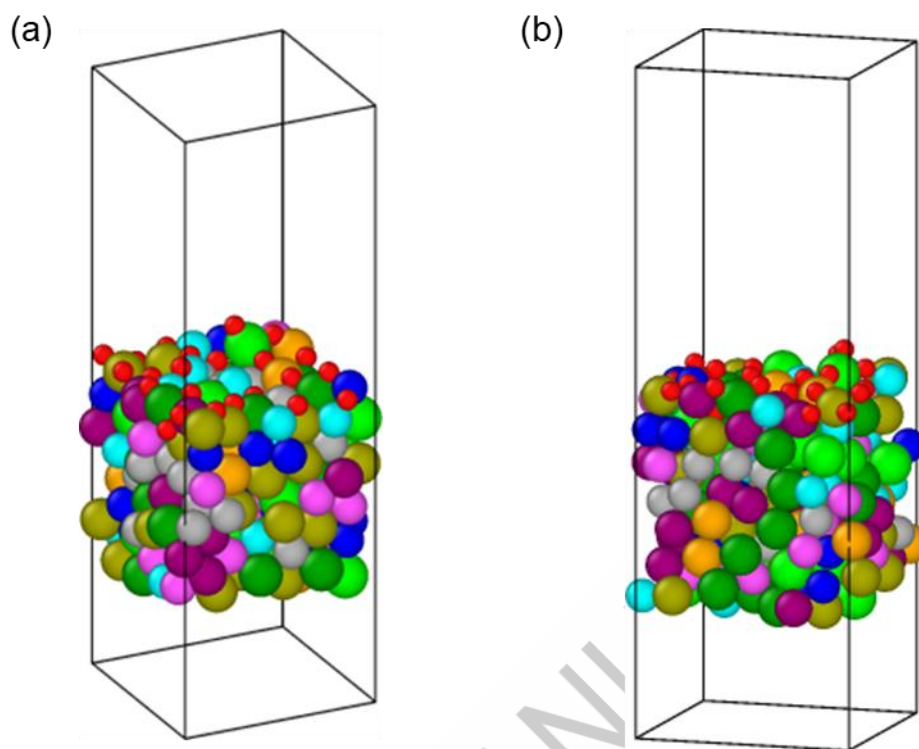
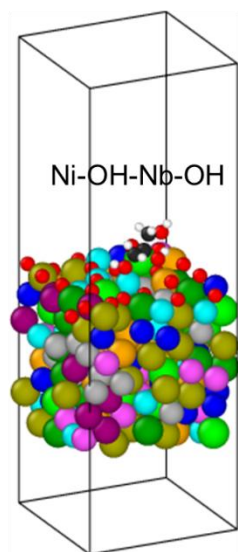
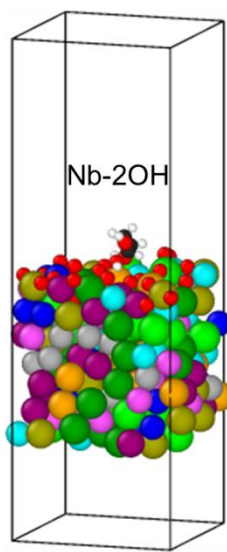


Figure S22. DFT calculation models of oxidized 9eHEA surface. (a) Ni-centered and (b) Nb-centered structural outline. Both models are same.

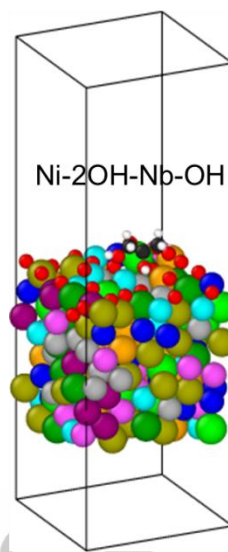
(a) -2.64 eV  
Double OH to surface



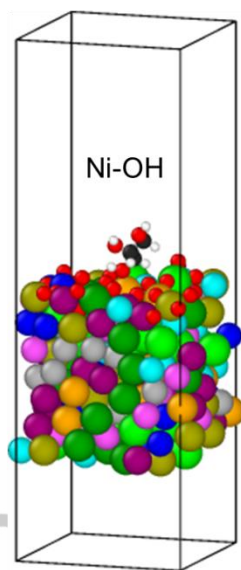
(b) -2.25 eV  
Double OH to surface



(c) -2.11 eV  
Triple OH on surface



(d) -1.77 eV  
Single OH to surface



(e) -1.57 eV  
single OH to surface

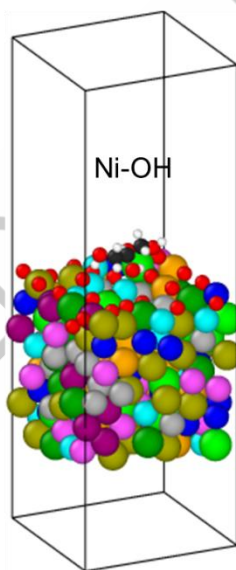


Figure S23. DFT calculations of glycerol adsorption (a) on Ni with single -OH (edge) and Nb with single -OH (center) as a bridge, (b) on Nb with double -OH (edge, center), (c) on Ni with double -OH and Nb with single -OH as a bridge, (d) on Nb with double -OH (edge, center), (e) on Ni with single -OH (edge) and (f) on Ni with single -OH (center) on the oxidized 9eHEA surface.

(a) -1.88 eV on Ni site parallel to surface (b) -2.87 eV on Ni site perpendicular to surface (c) -1.83 eV on Ni site parallel to surface (d) -2.82 eV on Ni site perpendicular to surface

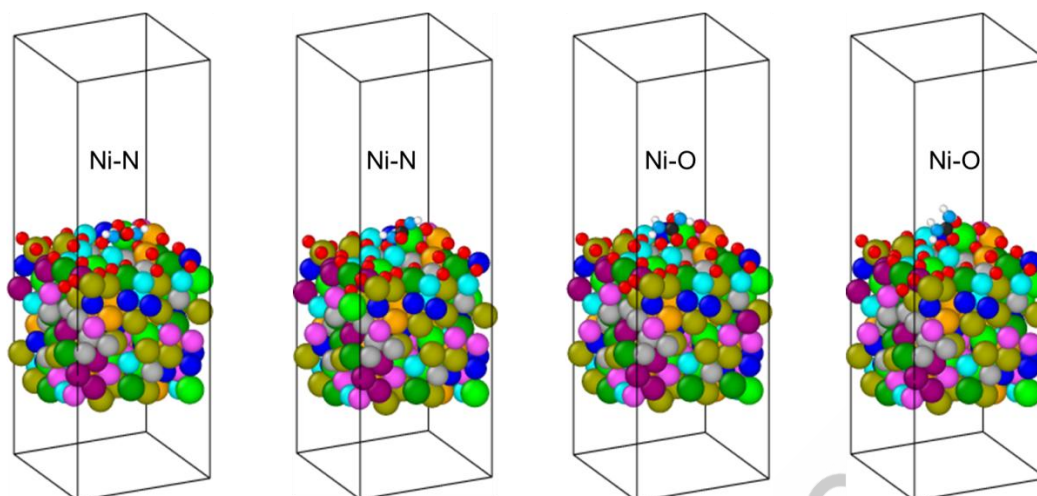


Figure S24. DFT calculations of urea adsorption (a) on Ni with  $\text{-NH}_2$  at a parallel position, (b) on Ni with  $\text{-NH}_2$  at a perpendicular position, (c) on Ni with  $\text{C=O}$  at a parallel position and (d) on Ni with  $\text{C=O}$  at a perpendicular position on the oxidized 9eHEA surface.

(a) -1.64 eV on Nb site parallel to surface    (b) -1.88 eV on Nb site perpendicular to surface    (c) -2.19 eV on Nb site parallel to surface    (d) -1.90 eV on Nb site perpendicular to surface

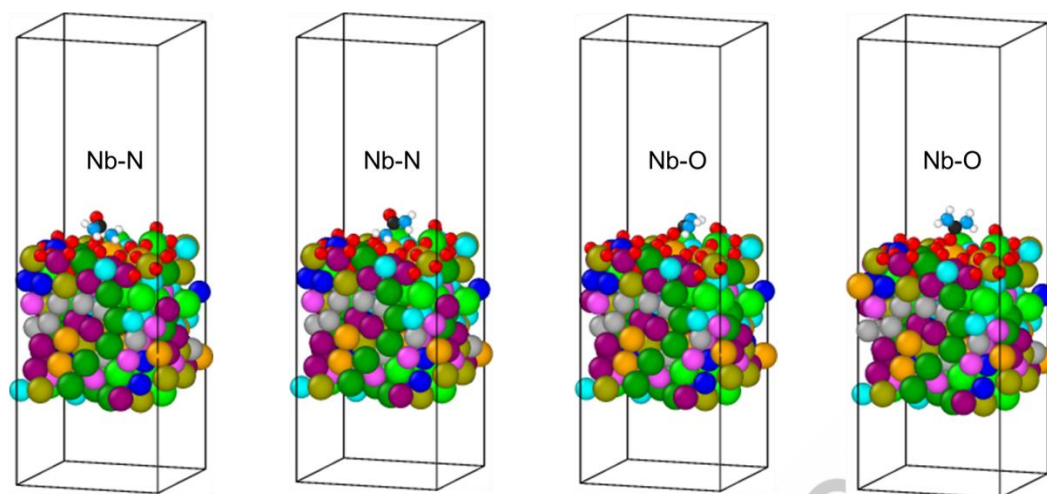


Figure S25. DFT calculations of urea adsorption (a) on Nb with  $\text{-NH}_2$  at a parallel position, (b) on Nb with  $\text{-NH}_2$  at a perpendicular position, (c) on Nb with  $\text{C=O}$  at a parallel position and (d) on Nb with  $\text{C=O}$  at a perpendicular position on the oxidized 9eHEA surface.

Table S1. Summary of electrochemical performance of 9eHEA anode tested in 0.5 M  $\text{H}_2\text{SO}_4$  electrolyte containing X-molecules and no X-molecule.

	$\eta_{10}$ (V)	$\eta_{100}$ (V)	Tafel slope (mV/dec)	$C_{dl}$ (mF/cm <sup>2</sup> )	$R_{ct}$ (Ohm)
No molecule	0.72	0.86	126	22.0	861
Methanol	0.70	0.85	125	22.4	590
Ethanol	0.71	0.87	126	26.4	620
Ethylene glycol	0.74	0.97	122	34.7	555
Glycerol	0.68	0.83	122	26.1	450
Formaldehyde	0.70	0.84	134	32.0	458
Acetaldehyde	0.70	0.86	133	21.2	760
Formic acid	0.71	0.87	134	24.9	590
Lactic acid	0.71	0.84	130	37.5	640
Urea	0.72	-	175	22.4	928
Biurea	0.68	0.85	156	33.8	780

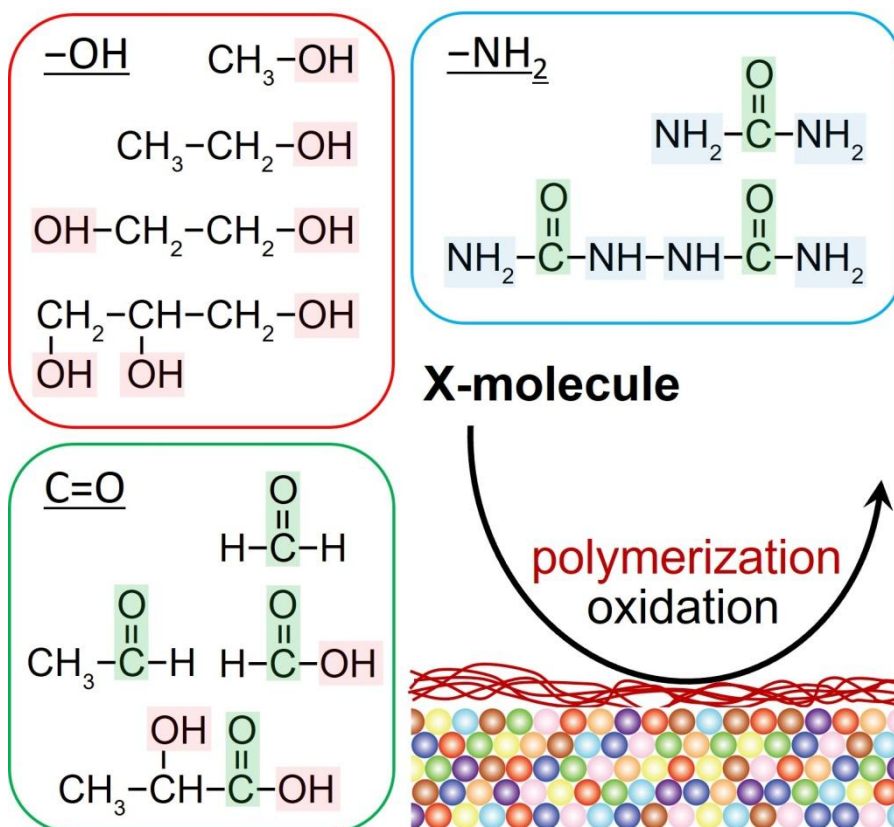
Table S2. Summary of atomic concentrations of 9eHEA anode before and after the test with and without X-molecules.

9eHEA with X-molecules after the CA test	Atomic concentration (at.%)								
	Ti	Cr	Mn	Fe	Co	Ni	Zr	Nb	Mo
acetaldehyde	10.6	12.8	11.0	12.8	11.8	11.1	10.7	11.5	7.9
biurea	9.9	13.2	10.8	12.7	11.5	10.2	10.2	11.7	9.9
ethylene glycol	7.8	12.0	6.5	11.6	9.6	7.4	9.8	13.3	22.0
ethanol	8.5	14.0	5.3	12.7	10.7	6.9	9.0	13.9	18.9
formaldehyde	11.0	11.5	9.2	10.5	9.0	8.0	11.9	14.1	14.7
formic acid	8.3	10.9	8.8	10.4	8.8	7.2	8.3	19.5	17.7
glycerol	8.2	14.9	12.5	13.7	10.5	7.4	9.6	12.5	10.8
methanol	9.2	13.7	3.2	13.1	10.6	8.1	9.8	13.5	19.0
lactic acid	8.4	13.8	10.5	12.7	10.6	8.5	9.7	12.2	13.5
urea	9.9	8.6	7.8	8.9	8.9	9.0	9.5	22.1	15.3
9eHEA without X- molecules	Atomic concentration (at.%)								
	Ti	Cr	Mn	Fe	Co	Ni	Zr	Nb	Mo
as-synthesized	10.8	11.0	8.3	11.6	12.3	11.8	10.9	11.4	11.9
after test	11.9	8.9	3.9	7.44	7.94	6.78	11.0	21.1	21.0

## References

- [S1] Jeong KJ, Miesse CM, Choi JH, et al. Fuel crossover in direct formic acid fuel cells, *Journal of Power Sources*. 2027;168:119–125. doi: 10.1016/j.jpowsour.2007.02.062
- [S2] Tajuddin AAH, Ohto T, Tanimoto H, et al. Toluene-Poisoning-Resistant High-Entropy Non-Noble Metal Anode for Direct One-Step Hydrogenation of Toluene to Methylcyclohexane. *ChemSusChem*. 2025;18(2):e202401071. doi: 10.1002/cssc.202401071
- [S3] Zhou W, Song J, Lin L, et al, *npj Computational Materials*, 2025;11:69. doi: 10.1038/s41524-025-01561-1
- [S4] Tajuddin AAH, Wakisaka M, Ohto T, et al. Corrosion-Resistant and High-Entropic Non-Noble-Metal Electrodes for Oxygen Evolution in Acidic Media. *Advanced Materials*. 2023;35(3):2207466. doi: 10.1002/adma.202207466





GraphicalAbstract1

## Impact Statement

This study investigated the electrochemical reactivity of various energy carriers and catalyst poisoning in acidic media, and also revealed the reaction mechanisms for electrolytic synthesis and fuel cell using energy carriers.

ACCEPTED MANUSCRIPT